

# Strangeness in the proton from $W$ +charm production and SIDIS data

Trey Anderson,<sup>1,2</sup> W. Melnitchouk,<sup>2</sup> and N. Sato<sup>2</sup>

<sup>1</sup>*Department of Physics, William & Mary, Williamsburg, Virginia 23185, USA*

<sup>2</sup>*Jefferson Lab, Newport News, Virginia 23606, USA*

**JAM Collaboration**

**(PDF Analysis Group)**

(Dated: January 3, 2025)

## Abstract

We perform a global QCD analysis of unpolarized parton distribution functions (PDFs) in the proton, including new  $W$ +charm production data from  $pp$  collisions at the LHC, which have been suggested for constraining the strange quark PDF. In particular, we assess the impact of the  $W$ +charm data relative to that of semi-inclusive pion and kaon production data in lepton-nucleon deep-inelastic scattering. Compared with a baseline global fit that does not include these datasets, we find that semi-inclusive deep-inelastic scattering and  $W$ +charm data combined favor a larger strange distribution, but smaller than the SU(3) symmetric sea suggested in previous analyses of ATLAS data. Combined, the ratio of strange to nonstrange sea quark distributions is  $R_s = (s + \bar{s})/(\bar{u} + \bar{d}) \approx \{0.72, 0.48, 0.26\}$  for  $x = \{0.01, 0.04, 0.1\}$ .

## I. INTRODUCTION

The simple picture of matter that has been built up over the past few decades of probing the femtometer scale structure of the proton attributes the bulk of its properties, such as baryon number, charge, or magnetic moment, to the irreducible core of its valence  $u$  and  $d$  quarks. In momentum space the distributions of these quarks have been mapped out in considerable detail from deep-inelastic scattering (DIS) and other high-energy scattering observables, over a large range of light-cone momentum fractions  $x$ . On top of this structure we now understand lies a teeming sea of virtual quark–antiquark pairs, which do not alter the global quantum numbers of the proton, but can affect some of its properties, such as the spin and magnetic moment, and yield nontrivial structures, such as an excess of antidown quarks over antiup,  $\bar{d} > \bar{u}$  [1–4], in the proton, and an analogous excess of  $\bar{u}$  in the neutron.

While expected to be suppressed because of its larger mass, the creation of strange–antistrange quark pairs is also expected to play a role in the femtoscopic structure of the proton. In ordinary matter, the creation of virtual  $u\bar{u}$  and  $d\bar{d}$  pairs is screened by the presence of the valence  $u$  and  $d$  quarks. Strange quarks, on the other hand, can directly reveal the properties of  $q\bar{q}$  pairs in the proton, although the practical realization of this has been severely hampered by the difficulty of obtaining reliable empirical information on the  $s$  and  $\bar{s}$  distributions in the proton. Although it is anticipated on general grounds that an asymmetry between  $s$  and  $\bar{s}$  quarks would be a unique window into the nonperturbative dynamics of quarks in the proton [5–7] (for example, in relation to the spontaneous breaking of chiral SU(3) symmetry), in practice even the magnitude of the sum  $s + \bar{s}$  is poorly known.

Historically, the shape of the strange quark PDF was first studied in neutrino-induced DIS from nuclear targets, particularly in the semi-inclusive production of charmed mesons in charged current reactions from the CCFR [8] and NuTeV [9] Collaborations at the Tevatron, as well as from the CHORUS [10] and NOMAD [11] experiments at CERN. An important complication in this process is the modeling of nuclear corrections in neutrino-nucleus DIS, which are currently poorly understood [12], and in the treatment of charm quark energy loss and charmed  $D$  meson-nucleon rescattering inside the nucleus [13]. An alternative avenue that avoids nuclear corrections is semi-inclusive DIS production of kaons, which depends on the strange quark PDFs and strange quark to kaon fragmentation functions (FFs) as an additional nonperturbative input. Attempts have been made to extract the  $s + \bar{s}$  distribution

from kaon SIDIS data by the HERMES Collaboration [14, 15] (see also Refs. [16–18]). More recently, inclusive  $W$  and  $Z$  boson production has been found to have sensitivity to the strange quark PDF, although mixed results have been obtained from measurements at ATLAS and CMS at the LHC [19–24]. Inclusive  $W$ +charm production in principle could have even greater sensitivity to the  $s$  and  $\bar{s}$  PDFs [25–27], in analogy with the neutrino DIS measurements, but still without the complications of nuclear targets.

Aside from the intrinsic value of understanding the structure of the proton sea, the precise determination of strange quark PDFs is key for extracting Standard Model parameters, such as the Cabibbo-Kobayashi-Maskawa matrix element  $V_{cs}$  and the weak mixing angle,  $\sin^2 \theta_W$ , as well as precision measurements on the mass of the  $W$ -boson that depend on precise knowledge of the strange quark PDF [28, 29]. In this paper, we revisit the question of the strange and antistrange quark distributions in the proton, with a new analysis that includes all of the above datasets involving proton beams and targets. For the first time we combine the inclusive and semi-inclusive DIS (SIDIS) structure functions and multiplicities, together with cross section ratios and charge asymmetries in  $W/Z$  and  $W$ +charm production in  $pp$  collisions at the LHC, simultaneously fitting PDFs and FFs to over 5000 data points. We compare and contrast the different pulls of the various datasets on the  $s$  and  $\bar{s}$  distributions, finding a general trend of an enhanced strangeness preferred by both SIDIS and  $W$ +charm data relative to the baseline, but still suppressed compared to some analyses of the ATLAS  $W$ +charm data [26]. Furthermore, we find that SIDIS data alone allow for a larger range of strangeness than when combined with the  $W$ +charm datasets.

We begin in Sec. II with a review of the theoretical framework used in this analysis, focusing on the new  $W$ +charm and SIDIS observables, and discussing the nonperturbative modeling for the PDFs and FFs. Section III provides a concise summary of the datasets used in the fit, including DIS, Drell-Yan lepton-pair production in  $pp$  and  $pd$  scattering,  $W^\pm$ ,  $Z$ ,  $W$ +charm, and jet production in  $pp$  or  $p\bar{p}$  reactions. The datasets also include pion, kaon, and charged hadron production in SIDIS, as well as single-inclusive  $e^+e^-$  annihilation. In Sec. IV, we discuss in detail our methodology for implementing the regression problem, including model calibration and the kinematical cuts applied to the data. We then present the results of the data-versus-theory comparisons and the extracted PDFs and FFs. Finally, conclusions are drawn in Sec. V, where we discuss future theoretical and experimental steps that could provide further insights into the strangeness content of the proton.

## II. THEORETICAL FRAMEWORK

The theoretical basis for this analysis is collinear QCD factorization, to fixed order in the QCD coupling  $\alpha_s$ , for various high-energy scattering processes which involve PDFs or FFs. These include DIS, Drell-Yan lepton-pair production, weak boson and jet production, and  $W + \text{charm}$  production, which directly constrain proton PDFs;  $\pi$ ,  $K$  and charged hadron production in SIA, which give information on FFs; and SIDIS, which depends on both PDFs and FFs. Since the focus of this study is specifically on the role of strangeness in the proton, we will discuss in greater detail the theoretical framework for processes most sensitive to the  $s$  and  $\bar{s}$  PDFs in the proton, namely, inclusive  $W + \text{charm}$  production in  $pp$  collisions and lepton-deuteron SIDIS. We also describe the parametrizations employed for our PDFs and FFs.

### A. Physical processes and factorization

The associated production of a  $W$  boson and a charm quark in  $pp$  collisions,

$$p + p \rightarrow W + c + X, \quad (1)$$

where  $X$  represents all other particles in the final state, is expected to be sensitive to the strange content of the proton. Here the charge state  $W^- + c$  originates from the scattering off a strange quark, while the  $W^+ + \bar{c}$  tags an antistrange quark. The  $c$  and  $\bar{c}$  quarks are identified within a jet by a muon produced from its semileptonic decay. Within the collinear factorization framework the differential cross section can be written as a convolution of the perturbatively calculated partonic cross section  $\hat{\sigma}_{a,b}^{W+c}$  and the nonperturbative PDFs  $f_a$  and  $f_b$  of partons  $a$  and  $b$  in the colliding protons,

$$\frac{d\sigma^{W+c}}{d|\eta|} = \sum_{a,b} \int \int_{x_a x_b} d\hat{x}_a d\hat{x}_b f_a(\hat{x}_a, \mu_F) f_b(\hat{x}_b, \mu_F) \hat{\sigma}_{a,b}^{W+c} \left( \frac{\hat{x}_a}{x_a}, \frac{\hat{x}_b}{x_b}, \mu_F, \mu_R \right), \quad (2)$$

where  $\eta$  is the pseudorapidity of the lepton from the  $W$ -boson decay. The PDFs are functions of the partonic momentum fraction variables  $\hat{x}_{a,b}$ , and  $x_{a,b}$  are related to the pseudorapidity by  $x_{a,b} = (M_W/\sqrt{s}) e^{\pm\eta}$ , with the sum in Eq. (2) running over parton flavors  $a$  and  $b$  for the contributing partonic channels. The partonic cross sections  $\hat{\sigma}_{a,b}^{W+c}$  is calculated at next-to-leading order (NLO) in the strong coupling  $\alpha_s(\mu_R)$  using the Monte Carlo

program MCFM [30], with the factorization scale  $\mu_F$  and renormalization scale  $\mu_R$  set to  $\mu_F = \mu_R = M_W$ .

For the SIDIS of a lepton  $\ell$  from a nucleon  $N$ , producing charged pions  $\pi^\pm$ , kaons  $K^\pm$  or unidentified hadrons,

$$\ell + N \rightarrow \ell + h^\pm + X, \quad (3)$$

the differential cross section can be written as the double convolution of the partonic cross section  $\hat{\sigma}_{a,b}^h$  with the PDF  $f_a$  and the parton  $b$  to hadron  $h$  FF  $D_b^h$ ,

$$\frac{d\sigma^h}{dx_B dz_h dQ^2} = \sum_{a,b} \int \int_{z_h, x_B} d\hat{x} d\hat{z} f_a(\hat{x}, \mu_F) D_b^h(\hat{z}, \mu_F) \hat{\sigma}_{a,b}^h\left(\frac{\hat{x}}{x_B}, \frac{\hat{z}}{z_h}, \mu_F, \mu_R, Q\right). \quad (4)$$

Here  $Q^2 \equiv -q^2$  is the squared four-momentum transfer to the nucleon,  $x_B = Q^2/2p \cdot q$  is the Bjorken scaling variable, with  $p$  and  $q$  the target nucleon and virtual photon four-momenta, respectively, and  $z_h = p \cdot p_h/p \cdot q$  is the fraction of the virtual photon's energy carried by the fragmenting hadron  $h$  with four-momentum  $p_h$ . The invariant mass squared of the unmeasured hadronic final state is given by  $W_{\text{SIDIS}}^2 = (p + q - p_h)^2$ . The partonic cross section  $\hat{\sigma}_{a,b}^h$  is evaluated perturbatively to NLO accuracy, and the factorization and renormalization scales are set as  $\mu_F = \mu_R = Q$ .

For all processes in our analysis we use the  $\overline{\text{MS}}$  scheme for the renormalization group equations, with the strong coupling  $\alpha_s$  evolved numerically using the QCD  $\beta$ -functions with the boundary condition  $\alpha_s(M_Z) = 0.118$  at the  $Z$ -boson mass,  $M_Z = 91.18$  GeV. The PDFs and FFs are evolved to next-to-leading logarithmic accuracy using the DGLAP evolution equations [31–33] in the zero-mass variable flavor scheme, setting the input scale to the charm quark mass,  $\mu = m_c$ , for both PDFs and FFs. The heavy quark mass thresholds are taken from PDG to be  $m_c = 1.28$  GeV and  $m_b = 4.18$  GeV [34].

## B. Nonperturbative modeling

We parameterize all PDFs at the input scale  $\mu^2 = m_c^2$  using the standard, phenomenologically successful template function

$$f(x, \mu; \mathbf{a}) = \frac{N}{\mathcal{M}} x^\alpha (1-x)^\beta (1 + \gamma\sqrt{x} + \delta x), \quad (5)$$

where the set of parameters to be fitted,  $\mathbf{a} = \{N, \alpha, \beta, \gamma, \delta\}$ , includes the normalization coefficient  $N$  and shape parameters  $\alpha$ ,  $\beta$ ,  $\gamma$  and  $\delta$ . To ensure that the normalization coefficient

$N$  is maximally decorrelated from the shape parameters, we normalize the function using  $\mathcal{M} = B[\alpha + 2, \beta + 1] + \gamma B[\alpha + \frac{5}{2}, \beta + 1] + \delta B[\alpha + 3, \beta + 1]$ , where  $B$  is the beta function (Euler integral of the first kind). The same form is used also for the FFs, with the parton momentum fraction  $x$  in Eq. (5) replaced by the momentum fraction  $z$  of the fragmenting parton.

As in most global QCD analyses, we assume isospin symmetry for the PDFs and FFs, so that a  $u$ -quark PDF in the proton is equivalent to a  $d$ -quark PDF in the neutron, for instance. For the PDFs, we parameterize the valence  $u$  and  $d$  quark distributions directly,

$$u_v \equiv u - \bar{u}, \quad d_v \equiv d - \bar{d}, \quad (6)$$

along with the gluon distribution,  $g$ , via Eq. (5). For the sea quark and antiquark distributions, we use the *ansatz*,

$$\begin{aligned} \bar{u} &= S_1 + \delta\bar{u}, & \bar{d} &= S_1 + \delta\bar{d}, \\ s &= S_2 + \delta s, & \bar{s} &= S_2 + \delta\bar{s}, \end{aligned} \quad (7)$$

where  $S_1$  and  $S_2$  play the role of the bulk of flavor-independent sea distribution for the light sea and strange sectors, respectively, while the quantities  $\delta f$  ( $f = \bar{u}, \bar{d}, s, \bar{s}$ ) are additional flavor dependent distortions away from  $S_{1,2}$  that are required to describe the observational data. Our modeling allows us to explore a range of possibilities for the sea distributions, including the symmetric sea scenario ( $S_1 = S_2$  and  $\delta f = 0$ ), light sea quark asymmetry, light and strange sea quark asymmetry, as well as the  $s - \bar{s}$  asymmetry. For the parametrizations of  $S_1, S_2$  and  $\delta f$  we use the same template function as in Eq. (5).

As usual, the normalization parameters for the  $u_v, d_v$ , and  $\delta s$  distributions are set using valence number sum rules,

$$\int_0^1 dx u_v = 2, \quad \int_0^1 dx d_v = 1, \quad \int_0^1 dx (s - \bar{s}) = 0, \quad (8)$$

while the normalization parameter for the gluon PDF is set by the momentum sum rule,

$$\int_0^1 dx x \left( \sum_q (q + \bar{q}) + g \right) = 1. \quad (9)$$

The parametrization template in Eq. (5) is also used for FFs, but with  $x$  replaced by  $z$ , the momentum fraction of the parton carried by the produced hadron. Assuming charge

symmetry, for the quark to  $\pi^+$  FFs we take

$$\begin{aligned} D_d^{\pi^+} &= D_{\bar{u}}^{\pi^+}, \\ D_u^{\pi^+} &= D_{\bar{d}}^{\pi^+}, \\ D_q^{\pi^+} &= D_{\bar{q}}^{\pi^+}, \quad q = s, c, b. \end{aligned} \tag{10}$$

For the  $q \rightarrow K^+$  FFs we allow the favored  $D_u^{K^+}$  and  $D_{\bar{s}}^{K^+}$  FFs to be independent, but set the FFs for the unfavored flavors to be equal,

$$\begin{aligned} D_d^{K^+} &= D_{\bar{u}}^{K^+} = D_{\bar{d}}^{K^+} = D_s^{K^+}, \\ D_q^{K^+} &= D_{\bar{q}}^{K^+}, \quad q = c, b, \end{aligned} \tag{11}$$

with the heavier charm and bottom quark and antiquark FFs also set equal to each other. For the unidentified charged hadron FFs, we follow the same parametrization used in the previous JAM FF analysis [35]. Namely, we use a residual term,  $D_q^{\text{res}+}$ , to parameterize the difference between the total charged hadron FF  $D_q^{h+}$  and the  $D_q^{\pi^+}$  and  $D_q^{K^+}$  functions, so that

$$D_q^{h+} = D_q^{\pi^+} + D_q^{K^+} + D_q^{\text{res}+}. \tag{12}$$

We also assume a SU(3) flavor symmetry for light quarks and antiquarks,

$$\begin{aligned} D_q^{\text{res}+} &= D_u^{\text{res}+} = D_d^{\text{res}+} = D_s^{\text{res}+}, \\ D_{\bar{q}}^{\text{res}+} &= D_{\bar{u}}^{\text{res}+} = D_{\bar{d}}^{\text{res}+} = D_{\bar{s}}^{\text{res}+}, \end{aligned} \tag{13}$$

The FFs for negatively charged hadrons are related by charge symmetry,  $D_q^{h-} = D_{\bar{q}}^{h+}$ , for all flavors  $q$ , with  $h = \pi, K, \text{res}$ .

### III. DATASETS

In this section we summarize the datasets that are used in the current global analysis. These include the standard baseline sets of DIS, Drell-Yan lepton-pair production, inclusive weak boson and jet production, as well as recent  $W$ +charm production data from the LHC. To facilitate better flavor separation of the PDFs, we utilize in addition SIDIS data from muon-deuterium scattering at COMPASS. Since the SIDIS process involves also FFs, we simultaneously fit these datasets together with single-inclusive  $e^+e^-$  annihilation (SIA) data, constraining the FF and PDF parameters self-consistently. The list of reactions and observables, and their associated connection to PDFs and FFs, is summarized in Table I.

TABLE I. Summary of processes, observables and their connection to PDFs and FFs.

Process	Observables	Cuts	PDFs/FFs
$\ell + (p, d) \rightarrow \ell' + X$	$F_2, \sigma_{\text{red}}$ [36–40]	$Q^2 > m_c^2$ $W^2 > 10 \text{ GeV}^2$	$f_{i/p}$
$\ell + d \rightarrow \ell' + (\pi^\pm, K^\pm, h^\pm) + X$	$dM^h/dz_h$ [41, 42]	$Q^2 > m_c^2$ , $W_{\text{SIDIS}}^2 > 10 \text{ GeV}^2$ $0.2 < z_h < 0.7$	$f_{i/p}$ $D_i^{(\pi^+, K^+, h^+)}$
$p + (p, d) \rightarrow \ell\bar{\ell} + X$	$d\sigma^{p/d}/dx_F dQ^2$ [2, 3]		$f_{i/p}$
$p + (p, \bar{p}) \rightarrow W + X$	$A_W, A_\ell, \sigma^{W^+}/\sigma^{W^-}$ [19–21, 23, 43–47]		$f_{i/p}$
$p + \bar{p} \rightarrow Z/\gamma^* + X$	$d\sigma/dy$ [48, 49]		$f_{i/p}$
$p + (p, \bar{p}) \rightarrow \text{jet} + X$	$d\sigma/d\eta dp_T$ [50–52]	$p_T > 8 \text{ GeV}$	$f_{i/p}$
$p + p \rightarrow W + c + X$	$d\sigma/d\eta$ [25–27]		$f_{i/p}$
$\ell + \bar{\ell} \rightarrow (\pi^\pm, K^\pm, h^\pm) + X$	$d\sigma/dz_h$ [53–68]	$0.2 < z_h < 0.9$	$D_i^{(\pi^+, K^+, h^+)}$

For inclusive DIS experiments, we use fixed-target data on proton and deuteron targets from SLAC [36], BCDMS [37], and NMC [38, 39], along with reduced neutral current and charged current proton cross sections for the combined H1 and ZEUS analysis of HERA collider data [40]. For the SIDIS measurements, we include data on pion, kaon, and unidentified charged hadron production on deuteron targets from the COMPASS Collaboration [41, 42]. We also note that in previous JAM analyses [35, 69] of the SIDIS data, one of the sources of systematic uncertainty was interpreted as a normalization uncertainty. This interpretation required a large fitted normalization to adequately describe the data. In the present analysis this uncertainty is instead interpreted as a point-to-point correlated systematic uncertainty, allowing the data to be well described without the need of a large fitted normalization for each dataset.

Drell-Yan lepton-pair production data from the E866 (NuSea) [2] and E906 (SeaQuest) [3]  $pp$  and  $pD$  scattering experiments at Fermilab are used to constrain mostly the  $\bar{d}/\bar{u}$  PDF ratio in the proton at small and intermediate values of  $x$ . Data for weak vector boson mediated processes including  $W$ -lepton asymmetries from the CMS [19–21, 23] and LHCb [43, 44]



Collaborations at the LHC, and the STAR [47] Collaboration at RHIC, along with  $W^\pm$  charge asymmetries and  $Z/\gamma^*$  rapidity distributions from CDF and D0 at the Tevatron [45, 46, 48, 49], are used to further constrain flavor separation including at high  $x$ . Jet production data from CDF and D0 [50, 51] and STAR [52] are also included, which are important for constraining the gluon PDF at large  $x$ . For  $W+$  charm quark production, which have been argued could be more sensitive to the strange quark PDFs, we use cross sections from the ATLAS [26] and CMS [25, 27] Collaborations at the LHC. SIA data involving pion, kaon, and unidentified charged hadron from the TASSO [53–55], ARGUS [68], TPC [56–58], HRS [59], SLD [61], BaBar [66], OPAL [63, 64], ALEPH [62], DELPHI [65], TOPAZ [60], and Belle [67] Collaborations are included to constrain the FFs.

The kinematic range covered by the data for each type of dataset and experiment is illustrated in Fig. 1. Here the scale  $Q^2$  is shown versus the Bjorken scaling variable  $x_B$  for DIS and SIDIS data, and versus the Feynman  $x_F$  variable for hadron-induced scattering reactions. In addition, for SIDIS and SIA data, the scale  $Q^2$  is shown versus the fragmentation variables  $z_h = p \cdot p_h / p \cdot q$  and  $z_h = 2p_h \cdot q / Q^2$ , respectively. The SIDIS data are critical, as these are the only datasets that have sensitivity to both the PDFs and FFs.

#### IV. GLOBAL QCD ANALYSIS

Having outlined the theoretical framework and data selection, in this section we present the results of our global QCD analysis. We emphasize that our analysis involves a simultaneous reconstruction of PDFs and FFs from all the considered datasets to leverage the quark flavor sensitivity of SIDIS datasets, while uniformly propagating uncertainties across all the involved distributions. We will first review the methodological aspects of our analysis, followed by a detailed description of our strategies for constructing posterior distributions for the PDFs and FFs.

The quality of the results will be discussed by examining the agreement between data and theory, with a focus on the impact of SIDIS multiplicities for  $\pi^\pm$ ,  $K^\pm$ , and unidentified hadron  $h^\pm$  production data from COMPASS, as well as  $W+$  charm production cross-section data from the LHC, on the magnitude and shape of the strange quark PDF. We discuss several scenarios, including the baseline results, which exclude SIDIS and  $W+$  charm data; two additional scenarios, where the baseline is supplemented with either SIDIS or  $W+$  charm

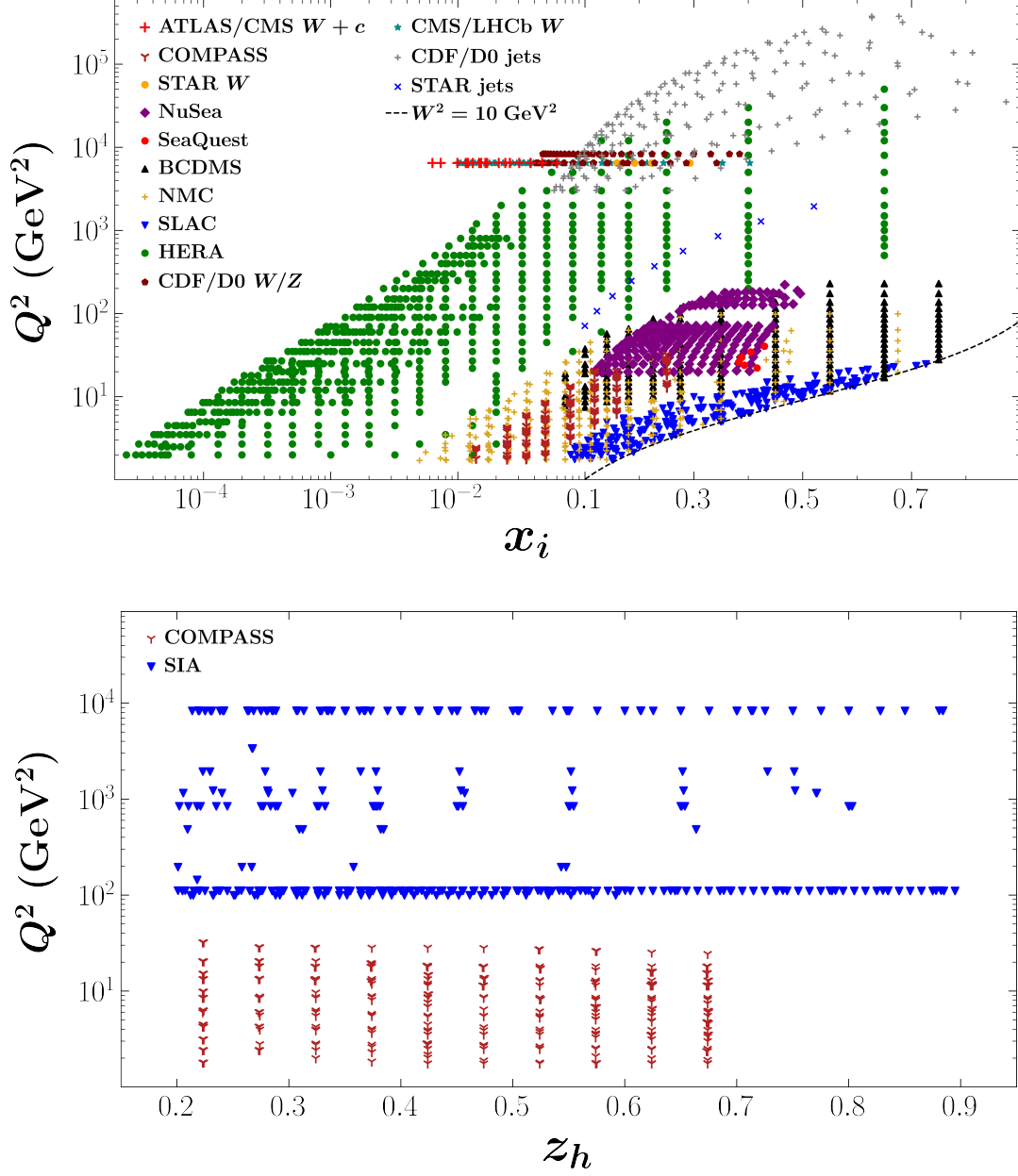


FIG. 1. Kinematic coverage of datasets used in this analysis, with the scale  $Q^2$  versus the Bjorken scaling variable  $x_i = x_B$  for DIS and SIDIS, and the Feynman variable  $x_i = x_F$  for Drell-Yan/weak boson/jet production data (upper panel), and the fragmentation variable  $z_h$  for SIDIS and SIA data (lower panel) are given as  $z_h = p \cdot p_h / p \cdot q$  and  $z_h = 2 p_h \cdot q / Q^2$  respectively.

data, respectively; and the final combined result, which incorporates all datasets in the analysis. We label these analyses as “baseline”, “+SIDIS”, “+W-charm”, and “JAM24”, respectively.

## A. Methodology and model calibration

The reconstruction of PDFs and FFs follows the multi-step Monte Carlo-based approach for Bayesian inference employed in previous JAM global QCD analyses [4, 35, 70]. This approach allows us to calibrate our models, quantify their performance across the parameter space, and mitigate overparametrization. The key algorithmic aspects of the methodology include the use of data resampling for optimization, and the multi-step strategy developed in Ref. [69].

In the current analysis several notable improvements have been introduced. First, the sea quark PDFs are initially treated as flavor symmetric during the steps prior to incorporating flavor sensitive experimental data. Once such data are added, they allow the separation of specific flavors from the total sea. This incremental approach enables a more reliable determination of PDF uncertainties by gradually introducing flavor asymmetries between sea quarks.

Second, we replace the initial flat prior distributions with Gaussian priors, choosing specific hyperparameters for each type of template parameter. We also include corresponding Gaussian penalties in the optimization procedure across the multi-steps to prevent the parameters from growing indefinitely and accumulating at parameter boundaries. In addition, the use of Gaussian penalties ensures the self-consistency of the template modeling (for example, the  $\gamma$  and  $\delta$  parameters in Eq. (5) should act as correction terms to the leading  $x^\alpha(1-x)^\beta$  term of the template function), and enables the specification of priors in extrapolation regions.

Lastly, when computing any physical observables from the MC parameter samples, we use the mean values as the central results, while uncertainties are estimated using Bayesian credible intervals at the 95% confidence level. Specifically, for any observable such as a PDF, FF, cross section or asymmetry, the edges of the confidence intervals are determined using a nonparametric estimate of the inverse cumulative distribution function [71].

With these improvements we proceed to perform model calibration for the baseline scenario, excluding the SIDIS and  $W$ +charm data. We initiate our multi-step optimization by first considering only DIS data, using a symmetric sea *ansatz*  $\delta\bar{u} = \delta\bar{d} = \delta s = \delta\bar{s} = 0$  and  $S_1 = S_2$ . The obtained posteriors are then used as priors for the next step in which DY data are added, and  $\delta\bar{u}$  and  $\delta\bar{d}$  allowed to vary away from zero. We continue the optimization by

incrementally extending the dataset to include  $W/Z$  and jet production data in subsequent steps. We perform an additional step where  $S_2$  is varied away from  $S_1$  and  $\delta\bar{s}$  is varied independently away from  $\delta\bar{s}$  in order to account for possible differences between the light and strange quark PDFs. The resulting MC replicas from this procedure constitute our baseline results.

During the optimization process of the baseline setup, we found that the  $\gamma$  and  $\delta$  parameters in Eq. (5) had little or no effect on the  $\delta s$ ,  $\delta\bar{s}$ , and  $S_2$  distributions. Consequently, these parameters were set to zero for these functions. However, they were allowed to vary freely for each of the  $u_v$ ,  $d_v$ ,  $g$ ,  $\delta\bar{u}$ ,  $\delta\bar{d}$ , and  $S_1$  distributions. This results in a total of 35 free parameters for the PDFs in the baseline analysis, comprising 30 shape parameters and 5 normalization parameters.

The model calibration for FFs is initially performed using only the SIA data. For pions and kaons we generally find it necessary to describe the data using two template shape functions for the  $u$  and  $d$  quark FFs, while the gluon and all other quark FFs are modeled with a single shape function. Due to the flexibility provided by the two shapes, the  $\gamma$  and  $\delta$  parameters are found to have no significant impact on describing the data and are therefore set to zero.

For the unidentified charged hadron FFs, the residual distributions are adequately modeled with a single shape function. In this case, the  $\alpha$ ,  $\gamma$ , and  $\delta$  parameters are kept the same for  $D_q^{\text{res}+}$  and  $D_{\bar{q}}^{\text{res}+}$ , while  $N$  and  $\beta$  are allowed to vary as free parameters. Overall, this results in 24 free FF parameters for each of  $\pi^+$  and  $K^+$  (8 normalization parameters and 16 shape parameters), and an additional 16 free parameters for residual hadrons (5 normalization parameters and 11 shape parameters).

As mentioned above, we consider different scenarios as extensions of the baseline fit. These include the addition of SIDIS data,  $W$ +charm data, and both SIDIS and  $W$ +charm data. Each scenario is implemented by performing additional steps, starting from the baseline results and incorporating the corresponding datasets. Importantly, the Gaussian penalties applied during the model calibration stages are removed in the final MC runs for each of the studied scenarios. The combined full analysis utilized 99 parameters to model the input scale PDFs and FFs, along with an additional 49 free normalization parameters for various datasets, bringing the total number of free parameters to be inferred from the data to 148.

## B. Figures of merit

As in previous JAM analyses, the optimization of the PDF and FF parameters against the data is performed using nuisance parameters. Specifically, a given experimental data point  $i$  from a dataset  $e$  with value  $d_{i,e}$  is compared against the corresponding factorization-based calculation  $T_{i,e}$ , with additional systematic distortions of the form:

$$T_{i,e} \rightarrow \widehat{T}_{i,e} \equiv \sum_k r_e^k \widetilde{\beta}_{i,e}^k + \frac{T_{i,e}}{N_e}, \quad (14)$$

where  $\widetilde{\beta}_{i,e}^k = (T_{i,e}/d_{i,e}) \beta_{i,e}^k$  represents the  $k$ -th rescaled source of point-to-point correlated systematic uncertainties, and  $\beta_{i,e}^k$  are the quoted correlated systematic uncertainties. The nuisance parameters  $r_e^k$  and  $N_e$  modify the original theory additively and multiplicatively, respectively, to best describe the data within the quoted systematic uncertainties. To avoid overfitting, the nuisance parameters are regulated with Gaussian penalties  $\sum_k (r_e^k)^2$  for the additive shifts and by  $(1 - N_e)^2/(\delta N_e)^2$  for the multiplicative shift, where  $\delta N_e$  is the quoted normalization uncertainty for experiment  $e$ .

The quantity  $\widehat{T}_{i,e}$  represents a modified theory that accounts for systematic biases present in the data, under the assumption that  $T_{i,e}$  is the correct underlying law for the reconstructed observable. In practice, however,  $T_{i,e}$  is only computable within the limits dictated by factorization theorems, the perturbative accuracy of the theoretical computation, and the expressivity of the nonperturbative modeling for PDFs and FFs. In this context, the deviations of  $\widehat{T}_{i,e}$  from  $T_{i,e}$ , which we can write symbolically as  $|\widehat{T} - T|$ , are not solely a measure of experimental biases, but also reflect the computational limitations of  $T_{i,e}$ . These include constraints from the theoretical framework and modeling assumptions. We therefore aim to minimize these deviations by adjusting our model assumptions, as will be discussed in Sec. [IV D](#) below in connection with the HERA charged current data.

To assess the quality of the global analysis, we utilize two figures of merit: the reduced  $\chi^2$  for each dataset, defined as

$$\chi_{\text{red}}^2 \equiv \frac{1}{N_{\text{dat}}} \sum_{i,e} \left( \frac{d_{i,e} - \text{E}[\widehat{T}_{i,e}]}{\alpha_{i,e}} \right)^2, \quad (15)$$

where  $\text{E}[\dots]$  is the expectation value, and the associated  $Z$ -score to evaluate the probabilities of the estimated  $\chi_{\text{red}}^2$ , taking into account the number of kinematical data points  $N_{\text{dat}}$  for each dataset. The quantities  $\alpha_{i,e}$  are the quadrature sums of all the quoted uncorrelated

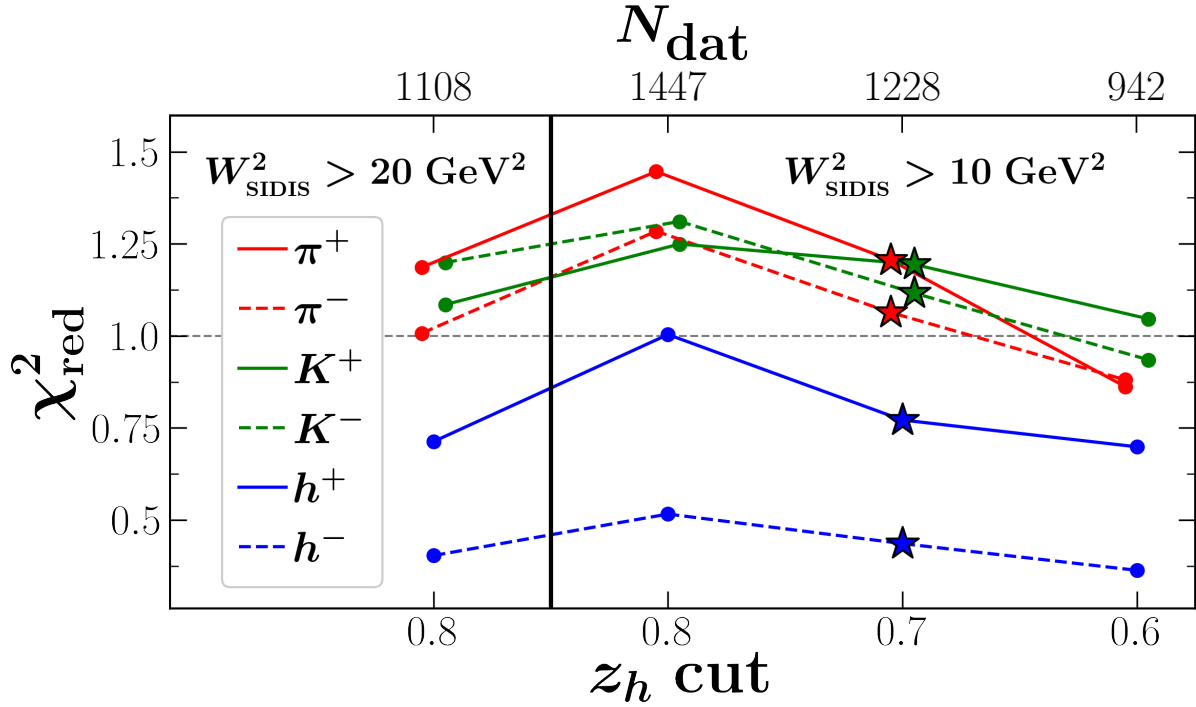


FIG. 2. Reduced  $\chi^2$  values for SIDIS data from COMPASS [41, 42] for pions (red lines), kaons (green lines) and unidentified charged hadrons (blue lines) for different  $W_{\text{SIDIS}}^2$  cuts ( $> 20 \text{ GeV}^2$  and  $> 10 \text{ GeV}^2$ ) and  $z_h$  cuts ( $< 0.8, 0.7$ , or  $0.6$ ), with the total number of remaining data points  $N_{\text{dat}}$  for each cut (top horizontal axis). The colored stars indicate the chosen  $W_{\text{SIDIS}}^2 > 10 \text{ GeV}^2$  and  $z_h < 0.7$  cuts used in the present analysis. The pion and kaon points are offset for clarity.

point-by-point uncertainties. The  $Z$ -score is defined in terms of the inverse of the normal cumulative distribution function,

$$Z = \Phi^{-1}(p) \equiv \sqrt{2} \operatorname{erf}^{-1}(2p - 1), \quad (16)$$

where the  $p$ -value is computed according to the  $\chi^2 \equiv N_{\text{dat}} \chi_{\text{red}}^2$  distribution with the number of data points  $N_{\text{dat}}$  as the degrees of freedom.

### C. Data selection

For DIS datasets, we apply the kinematic cuts  $W^2 > 10 \text{ GeV}^2$  and  $Q^2 > m_c^2$  to avoid the nucleon resonance region, and suppress higher twist corrections to the leading twist approximations to the structure functions. For the SIDIS data, we also studied the effect

that various cuts on  $W_{\text{SIDIS}}^2$  and  $z_h$  have on the description of the data. To compute  $W_{\text{SIDIS}}^2$ , it is necessary to specify the hadron transverse momentum in the Breit frame,  $p_{hT}$  [72]. Since the SIDIS cross sections receive most of their contributions from regions with small transverse momentum, we set its value to zero when evaluating  $W_{\text{SIDIS}}^2$ .

A cut on  $W_{\text{SIDIS}}^2$  allows one to isolate a region where higher twist and target mass corrections can be neglected, while a cut on  $z_h$  avoids the need for large- $z$  threshold corrections. In Fig. 2, we show the SIDIS  $\chi_{\text{red}}^2$  for various  $W_{\text{SIDIS}}^2$  and  $z_h$  cuts, along with the total number of data points remaining after the cuts are applied. While the  $W_{\text{SIDIS}}^2 > 10 \text{ GeV}^2$  and  $z_h < 0.6$  cuts allow for the best overall description of the data, the cuts would result in an almost 40% reduction of the number of data points relative to previous JAM analyses [35, 69]. Instead, we find that data within the kinematic cuts  $Q^2 > m_c^2$  and  $z_h < 0.7$ , with  $W_{\text{SIDIS}}^2 > 10 \text{ GeV}^2$ , could still be well described, while retaining the maximum number of data points in the global fit. Similarly for SIA, to avoid large perturbative effects at small and large values of  $z_h$ , we restrict the data to the range  $0.2 < z_h < 0.9$  to give the maximal overlap with the SIDIS dataset kinematics.

#### D. Data versus theory comparison

A summary of the figures of merit is presented in Table II and Fig. 3, respectively, for the three scenarios discussed in this work. Starting with the baseline scenario, we find that all datasets considered in the analysis are described quite well. An exception is the neutral current  $e^\pm p$  HERA data at  $\sqrt{s} = 318 \text{ GeV}$ . The  $Z$ -scores for this dataset are relatively high, with  $\chi_{\text{red}}^2 = 1.51$  and  $Z = 6.25$  for  $e^+p$ , and  $\chi_{\text{red}}^2 = 1.58$  and  $Z = 4.44$  for  $e^-p$  scattering, indicating potential difficulties in describing the DIS data across the full range of HERA kinematics.

Since the uncertainties are typically larger at higher  $x$ , it is likely that the observed tensions occur at small  $x$ , where higher-order  $\log x$  corrections are known to play a more important role. We have verified this hypothesis by performing the analysis with a larger  $Q^2$  cut,  $Q^2 > 3.5 \text{ GeV}^2$ , to remove data with  $x$  values  $x < 3.46 \times 10^{-5}$ . The results, shown in Fig. 3 as open circles, demonstrate that the  $Z$ -score can be reduced from 6.32 to as low as 4.34.

To test whether the tensions in the HERA data may be lessened by increasing the per-

TABLE II. Reduced  $\chi_{\text{red}}^2$  and  $Z$ -score values for each of the four scenarios considered in this analysis (with the total number of data points for each): baseline (3800 data points), +SIDIS (5028), + $W$ -charm (3837), and the full JAM24 analysis (5065). The  $N_{\text{dat}}$  values listed in the table for each type of observable correspond to the JAM24 fit.

Process	$N_{\text{dat}}$	$\chi_{\text{red}}^2$ ( $Z$ -score)			
		baseline	+SIDIS	+ $W$ -charm	<b>JAM24</b>
DIS					
fixed target [36–39]	1495	1.06 (1.66)	1.07 (1.95)	1.06 (1.52)	<b>1.07 (1.91)</b>
HERA [40]	1185	1.27 (6.02)	1.29 (6.40)	1.26 (5.97)	<b>1.28 (6.32)</b>
Drell-Yan [2, 3]	205	1.14 (1.36)	1.16 (1.61)	1.14 (1.41)	<b>1.16 (1.53)</b>
$W$ -lepton asymmetry [19–21, 23, 43, 44, 47]	70	0.83 (−1.02)	0.92 (−0.44)	0.81 (−1.11)	<b>0.87 (−0.77)</b>
$W$ charge asymmetry [45, 46]	27	1.00 (0.08)	1.15 (0.62)	1.01 (0.12)	<b>1.01 (0.13)</b>
$Z$ rapidity [48, 49]	56	1.05 (0.33)	1.05 (0.33)	1.10 (0.57)	<b>1.08 (0.46)</b>
Inclusive jets [50–52]	198	0.97 (−0.32)	0.96 (−0.35)	0.97 (−0.24)	<b>0.95 (−0.49)</b>
$W$ + charm [25–27]	37	— (—)	— (—)	0.64 (−1.73)	<b>0.75 (−1.08)</b>
SIDIS					
$\pi^\pm$ [41]	410	— (—)	1.12 (1.64)	— (—)	<b>1.14 (1.92)</b>
$K^\pm$ [42]	408	— (—)	1.17 (2.29)	— (—)	<b>1.15 (2.11)</b>
$h^\pm$ [41]	410	— (—)	0.61 (−6.48)	— (—)	<b>0.61 (−6.61)</b>
SIA					
$\pi^\pm$ [53–68]	231	0.91 (−0.32)	0.90 (−1.07)	0.91 (−0.32)	<b>0.91 (−0.92)</b>
$K^\pm$ [53–55, 57–68]	213	0.51 (−6.26)	0.80 (−2.20)	0.51 (−6.26)	<b>0.79 (−2.32)</b>
$h^\pm$ [53–55, 58, 61–65]	120	0.73 (−2.31)	0.93 (−0.52)	0.73 (−2.31)	<b>0.95 (−0.34)</b>
<b>Total</b>	<b>5065</b>	1.07 (2.82)	1.07 (3.49)	1.08 (3.35)	<b>1.07 (3.26)</b>

turbative accuracy of our (NLO) analysis, we compare in Table III the results from the NNLO analyses by NNPDF [73] and CT18 [74]. The comparison indicates that our results are similar to those obtained by these groups. In particular, we find that applying a larger



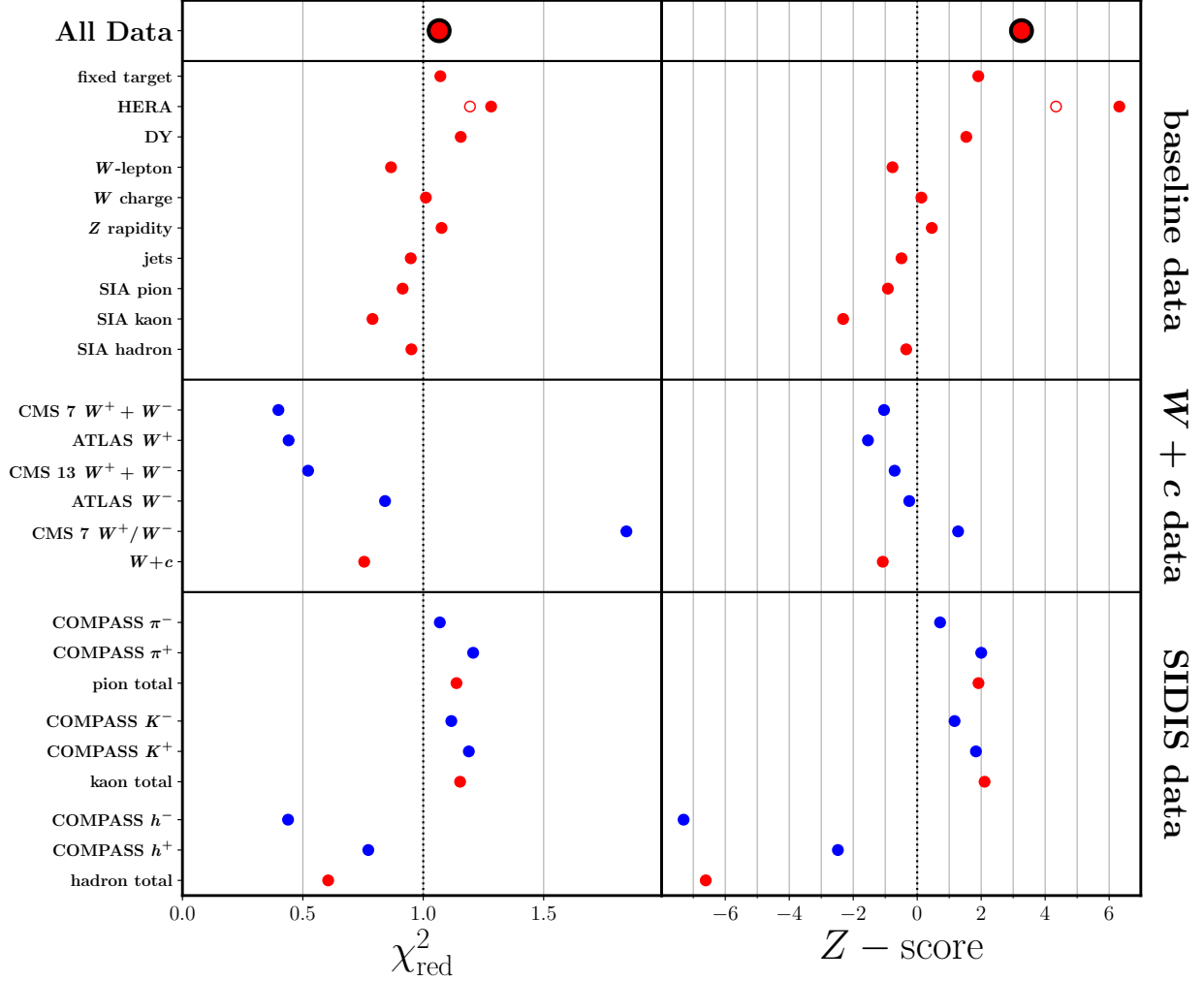


FIG. 3.  $\chi^2_{\text{res}}$  and  $Z$ -score values of all datasets used in the current analysis, including for the baseline datasets (top panel),  $W$ +charm data from CMS and ATLAS (middle panel), and SIDIS  $\pi^\pm$ ,  $K^\pm$ , and  $h^\pm$  production from COMPASS (bottom panel). The reduced  $\chi^2$  for individual datasets and averages over datasets are indicated by the blue and red points, respectively, and an additional open circle shows the reduced  $\chi^2$  and  $Z$ -score of the HERA data using for  $Q^2 > 3.5 \text{ GeV}^2$  cut.

$Q^2$  cut, as in the NNPDF analysis [73], yields  $\chi^2_{\text{red}}$  and  $Z$ -score values very similar to our results.

Moreover, we have verified that our reconstructed PDFs and FFs are not significantly affected by the value of the DIS cut. However, since our primary objective is to study the reconstruction of the strange quark PDF from SIDIS and  $W$ +charm data — and because applying a  $Q^2 > 3.5 \text{ GeV}^2$  to SIDIS would remove a significant amount of data — we retain

TABLE III. Comparisons of the reduced  $\chi_{\text{red}}^2$  and  $Z$ -score values for HERA inclusive DIS data for the JAM24 global analysis with the NNPDF4.0 [73] and CT18 [74] fits.

Analysis	pQCD accuracy	$Q_{\text{cut}}^2$ (GeV <sup>2</sup> )	$N_{\text{dat}}$	$\chi_{\text{red}}^2$	$Z$ -score
NNPDF4.0 [73]	NNLO	3.49	1145	1.17	3.89
CT18 [74]	NNLO	4.0	1120	1.30	6.51
JAM24	NLO	3.5	1120	1.19	4.34
	NLO	$m_c^2$	1185	1.28	6.32

our nominal  $Q^2 > m_c^2$  cut as the final choice for all scenarios.

We observe that the inclusion of the SIDIS datasets in the +SIDIS scenario tends to slightly increase the figures of merit, with the most notable case being the  $W$  charge asymmetry, which can modify the light sea quark PDFs. However, the changes in  $Z$ -scores are mostly within  $1\sigma$ , with the exception of SIA charged hadrons, which shifts from  $-2.31$  to  $-0.52$ , but still remains acceptable. Overall, we do not observe significant tensions when combining SIDIS data with the rest of the global dataset considered in our analysis.

The case of SIDIS charged hadrons is somewhat anomalous, with a  $Z$ -score of  $-6.61$ . This indicates that its uncertainties are dominated by correlated systematic errors, and that the data are not Gaussianly distributed around the reconstructed underlying physical law. Nevertheless, its description remains acceptable, as the reduced  $\chi^2$  is nominally below unity.

The figures of merit with the inclusion of  $W$ +charm data in the + $W$ -charm scenario are largely compatible with the baseline results. For the  $W$ +charm datasets, both the ATLAS and CMS cross sections are well described, with  $\chi_{\text{red}}^2 < 1$ , except for the CMS  $W$ +charm ratio measurement, which has a  $\chi_{\text{red}}^2 = 1.84$ . However, the relatively low  $Z$ -score of 1.28 does not indicate an anomaly.

Focusing on the main datasets of interest for the current analysis, a detailed comparison between theory and data for the ATLAS and CMS  $W$ +charm production cross sections, differential in the lepton pseudorapidity  $|\eta_\ell|$ , is shown in Fig. 4 for various values of the lepton transverse momentum lower cutoff,  $p_T^\ell$ . For all of the CMS  $W$ +charm cross sections, as well as the ATLAS  $W^+ + \bar{c}$  data, excellent overall agreement is seen for both the 7 TeV and 13 TeV experimental data. For the ATLAS  $W^- + c$  data, the theory slightly underestimates

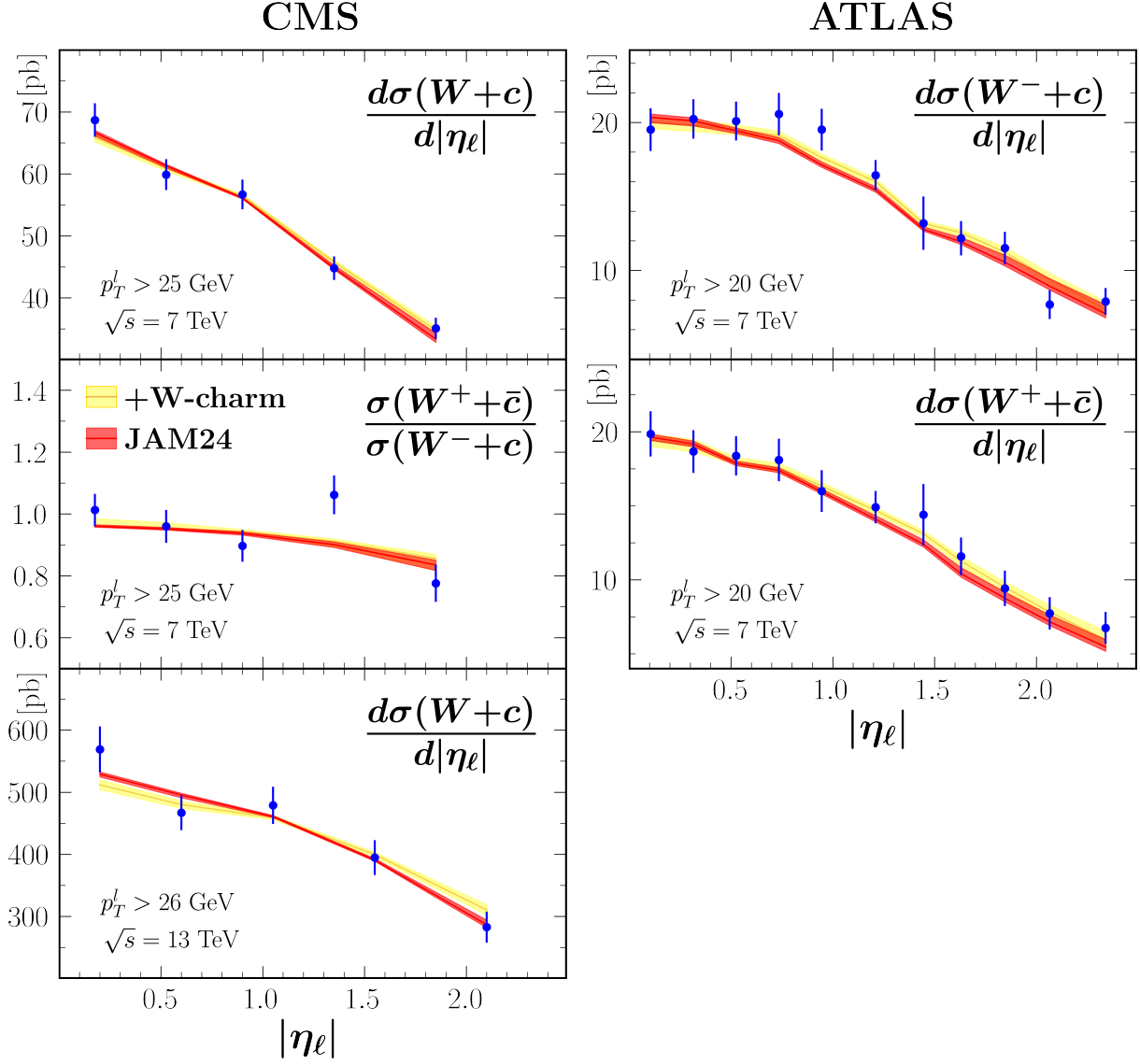


FIG. 4. Comparison between  $W$ +charm experimental data and the JAM24 global analysis versus lepton pseudorapidity,  $|\eta_\ell|$ , with 95% credible interval uncertainty bands. (Left): Sum (top) and ratio (middle) at 7 TeV [25], and sum (bottom) at 13 TeV [27] of  $W^+ + \bar{c}$  and  $W^- + c$  cross sections from CMS. (Right): Differential cross section of  $W^- + c$  (top) and  $W^+ + \bar{c}$  (middle) from ATLAS at 7 TeV [26]. The cuts on the transverse momentum of the final state lepton  $p_T^\ell$  are indicated on the panels.

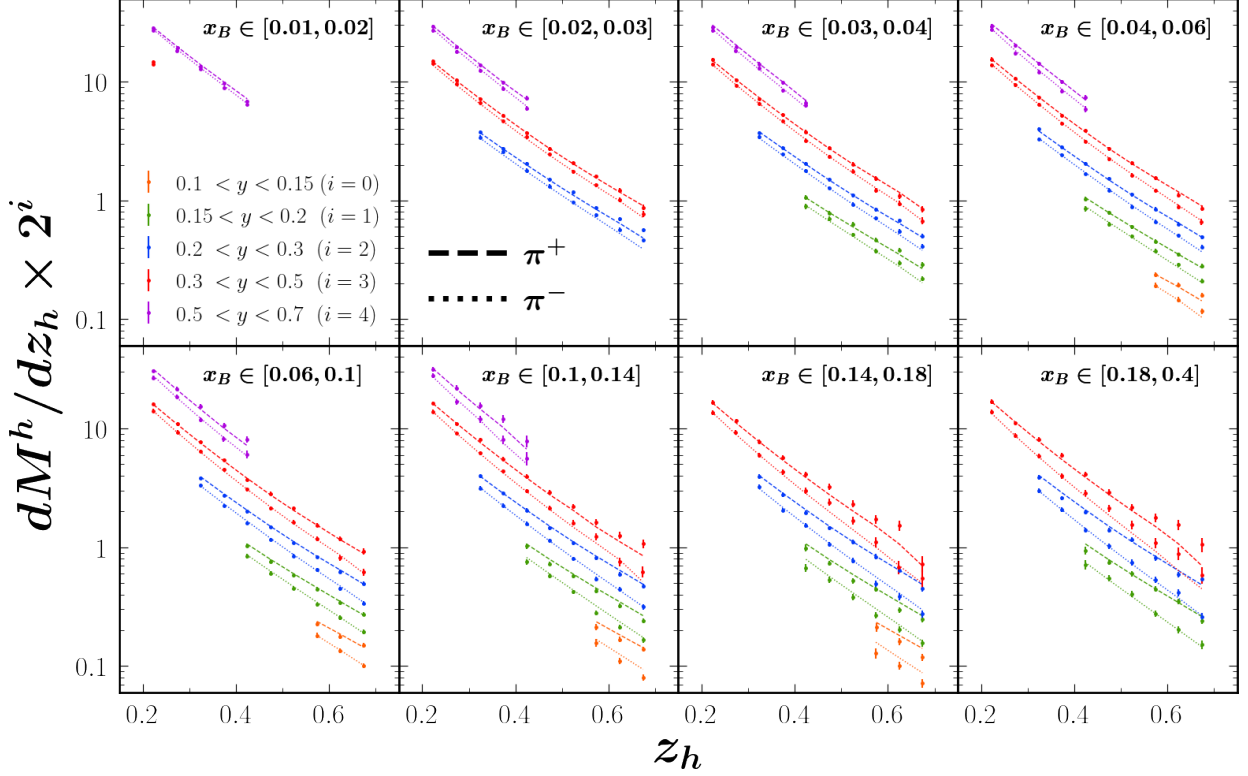


FIG. 5. SIDIS multiplicities  $dM^h/dz_h$  from COMPASS [41] as a function of  $z_h$  for  $h = \pi^+$  (dashed lines) and  $h = \pi^-$  (dotted lines) compared with the JAM24 fit result. The data and curves are scaled by a factor of  $2^i$  ( $i = 0, \dots, 4$ ) to more clearly separate and isolate the various  $x_B$  and  $y$  bins.

the measurements at  $|\eta_\ell| \sim 0.8$ , while for the CMS  $(W^+ + \bar{c})/(W^- + c)$  ratio the description at  $|\eta_\ell| = 1.35$  differs by  $2.5\sigma$ , leading to a larger  $\chi^2_{\text{red}}$  than for the other datasets.

Both the ATLAS and CMS data indicate a slightly larger  $W^- + c$  cross section compared with that for  $W^+ + \bar{c}$ . This would indicate a positive strange-antistrange asymmetry,  $s - \bar{s}$ , arising from a small preference of the  $gs \rightarrow W^- + c$  channel versus the  $g\bar{s} \rightarrow W^+ + \bar{c}$  channel. However, this conclusion is still somewhat limited by the current experimental uncertainties, and additional, higher precision data would be needed to make more definitive statements.

Turning now to the SIDIS data from COMPASS, in Figs. 5, 6, and 7 we show the  $z_h$  dependence of the  $\pi^\pm$ ,  $K^\pm$ , and  $h^\pm$  multiplicities, respectively, defined as ratios of cross sections for SIDIS and inclusive DIS at the same values of  $x_B$  and  $Q^2$ ,

$$\frac{dM^h}{dz_h} = \frac{d\sigma^h/dx_B dz_h dQ^2}{d\sigma^{\text{DIS}}/dx_B dQ^2}. \quad (17)$$

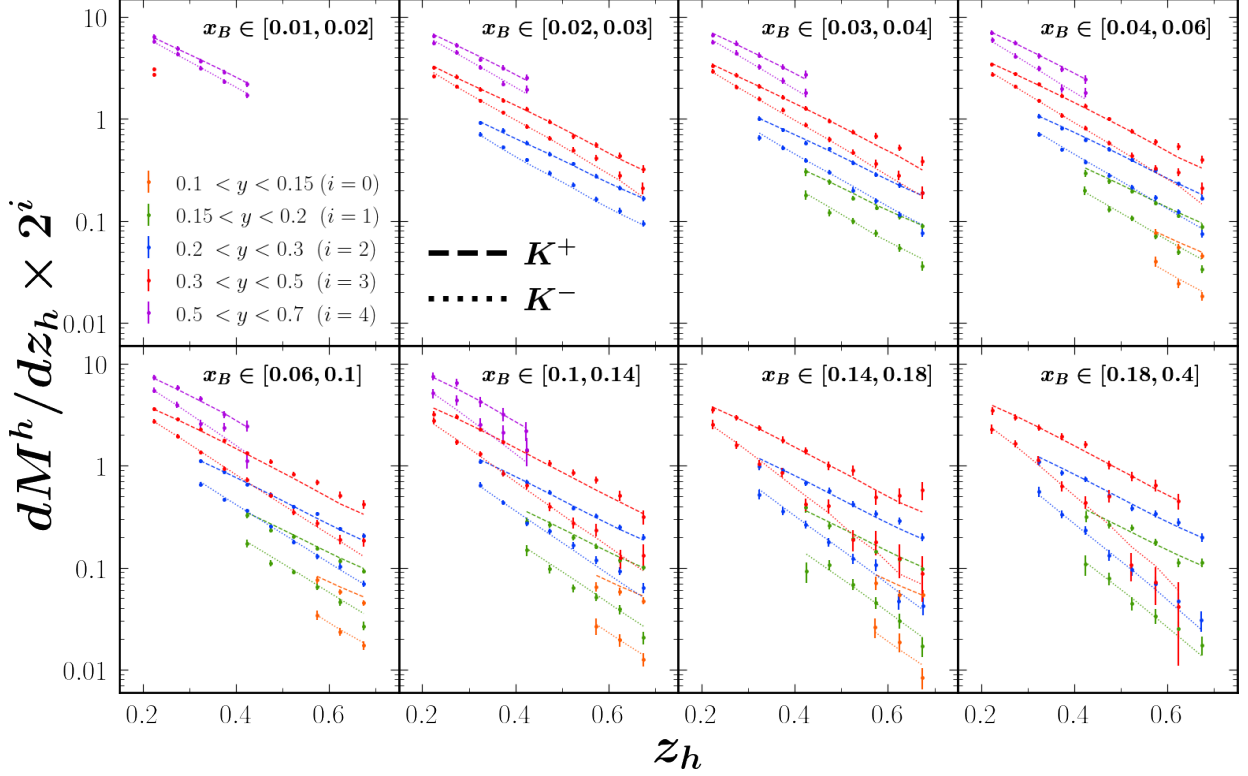


FIG. 6. As in Fig. 5, but for  $K^\pm$  data.

For all hadrons, better agreement between theory and experimental data is found for negatively charged hadrons than for positively charged hadrons. This can be observed in both the high- $x_B$  and low- $Q^2$  (low- $y$ ) regions, where the differences in the positively and negatively charged hadron multiplicities become larger, especially for kaons. In general, a good description of the COMPASS data is obtained across most kinematic regions and bins, with poorer agreement in the high- $z_h$  region and the low- $Q^2$  region for some higher- $x_B$  bins. Better agreement may be obtained by including hadron mass and other power corrections [75–77], which are known to be more important at large  $x_B$  and large  $z_h$ , as one approaches the exclusive limit.

For completeness, we also present in Fig. 8 the data and theory comparisons for DY datasets from the NuSea and SeaQuest experiments, as well as the  $W$ -lepton cross section ratios from STAR, demonstrating an excellent description of these data within the JAM24 scenario. While these datasets are not directly sensitive to the strange quark PDF, they do provide constraints on the light sea sector, particularly the  $\bar{d} - \bar{u}$  asymmetry. Changes

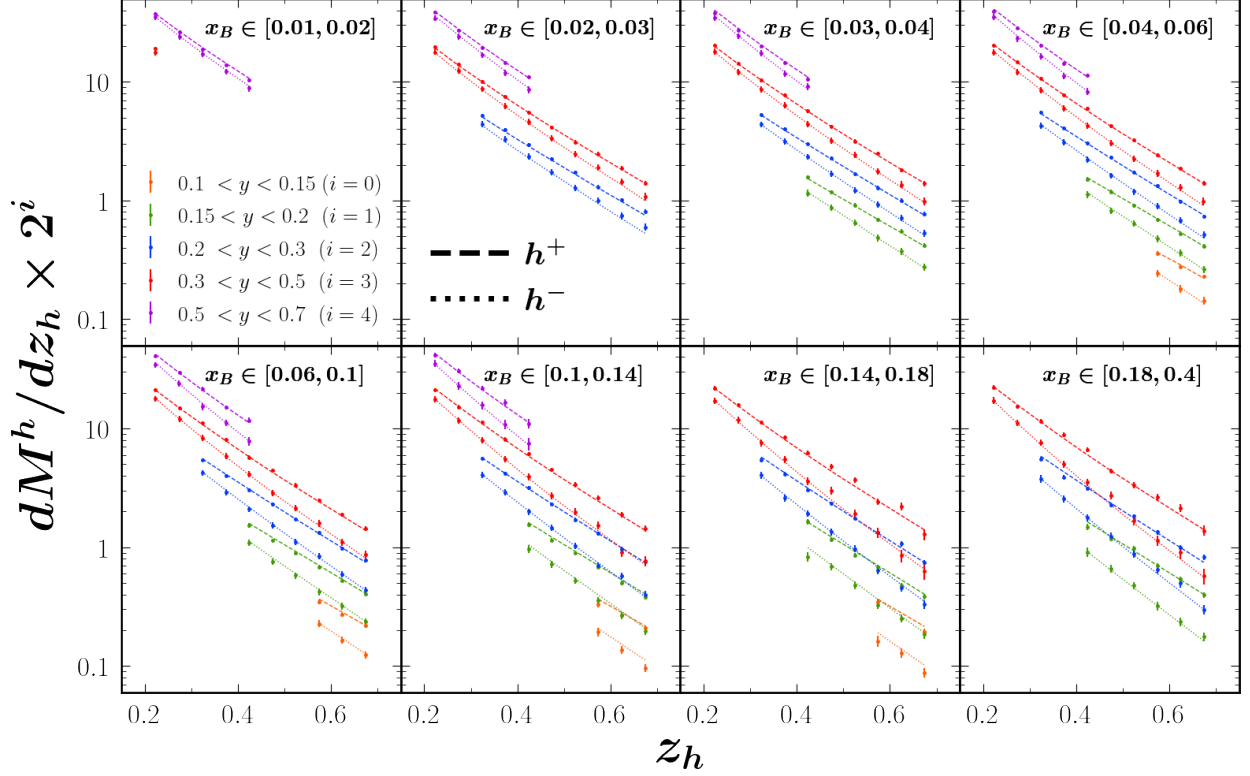


FIG. 7. As in Fig. 5, but for unidentified hadrons  $h^\pm$ .

in the light sea quark sector can, however, induce modifications in the strange quark PDF through QCD evolution and the overall description of the global dataset.

Lastly, we address the impact of adopting different small- $x$  asymptotic behaviors for the light sea and strange quark PDFs, modeled using the two independent functions,  $S_1$  and  $S_2$ , in Eq. (7). During the model calibration, we observed differences in the charged current data from HERA by contrasting the results for  $S_1 \neq S_2$  and  $S_1 = S_2$ . While both cases provide equally good descriptions of the data, we found that  $S_1 = S_2$  describes the data with larger systematic corrections. This effect is illustrated in Fig. 9, where the systematic corrections,  $|\hat{T} - T|$ , discussed in Sec. IV B above, are larger near the edges of the phase space for the  $S_1 = S_2$  case. This indicates that the charged current data prefer an asymmetry between the light sea and strange quark sectors at small  $x$ , which would otherwise be absorbed by the nuisance parameters. We therefore adopt  $S_1 \neq S_2$  in all the scenarios explored in this work.

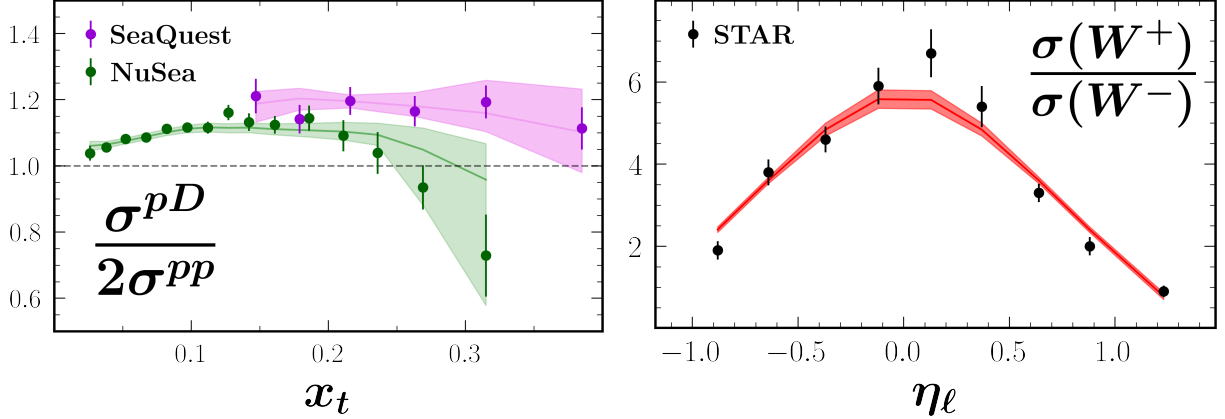


FIG. 8. (Left) Ratio of  $pD$  to  $pp$  Drell-Yan cross sections versus the target momentum variable  $x_t$  from SeaQuest (purple circles) for  $0.48 < x_b < 0.69$  and NuSea (green circles) for  $0.32 < x_b < 0.56$ , compared to the JAM24 fit result (colored bands). (Right)  $W$ -lepton ratio cross sections for  $pp$  collisions from STAR at  $\sqrt{s} = 510$  GeV and  $p_T^\ell > 25$  GeV as a function of pseudorapidity  $\eta_\ell$  compared to the JAM24 fit (red band).

### E. Reconstructed PDFs and FFs

Having established the agreement between our fits and the data, we now present the reconstructed PDFs and FFs in the various scenarios, focusing in particular on understanding the impact of the SIDIS and  $W+$  charm data on both the magnitude and constraints of the strange quark PDF. The effects of the additional datasets beyond the baseline on the strange and light antiquark distributions are illustrated in Fig. 10, where results for the starting baseline, +SIDIS, + $W$ -charm, and the final JAM24 fit that incorporates both SIDIS and  $W+$  charm datasets are compared at a common scale of  $Q^2 = 4$  GeV<sup>2</sup>.

We observe a clear tendency for the inclusion of SIDIS or  $W+$  charm data to increase the net strange quark content,  $s^+ = s + \bar{s}$ , beyond the baseline fit uncertainties for  $x \lesssim 0.1$ , while keeping the light sea distributions compatible with the baseline results within uncertainties. The  $W+$  charm data tend to increase  $s^+$  around  $x = 0.1$ , resulting in an approximately constant behavior for the ratio of strange to nonstrange sea quark PDFs,  $R_s = (s + \bar{s})/(\bar{u} + \bar{d})$ , particularly in the intermediate- $x$  region. However, the increased  $R_s$  remains incompatible with an SU(3)-symmetric light-quark sea across all  $x$ , as reported by the ATLAS Collaboration [26]. This discrepancy may arise due to dataset limitations or

## HERA CC $e^+p$

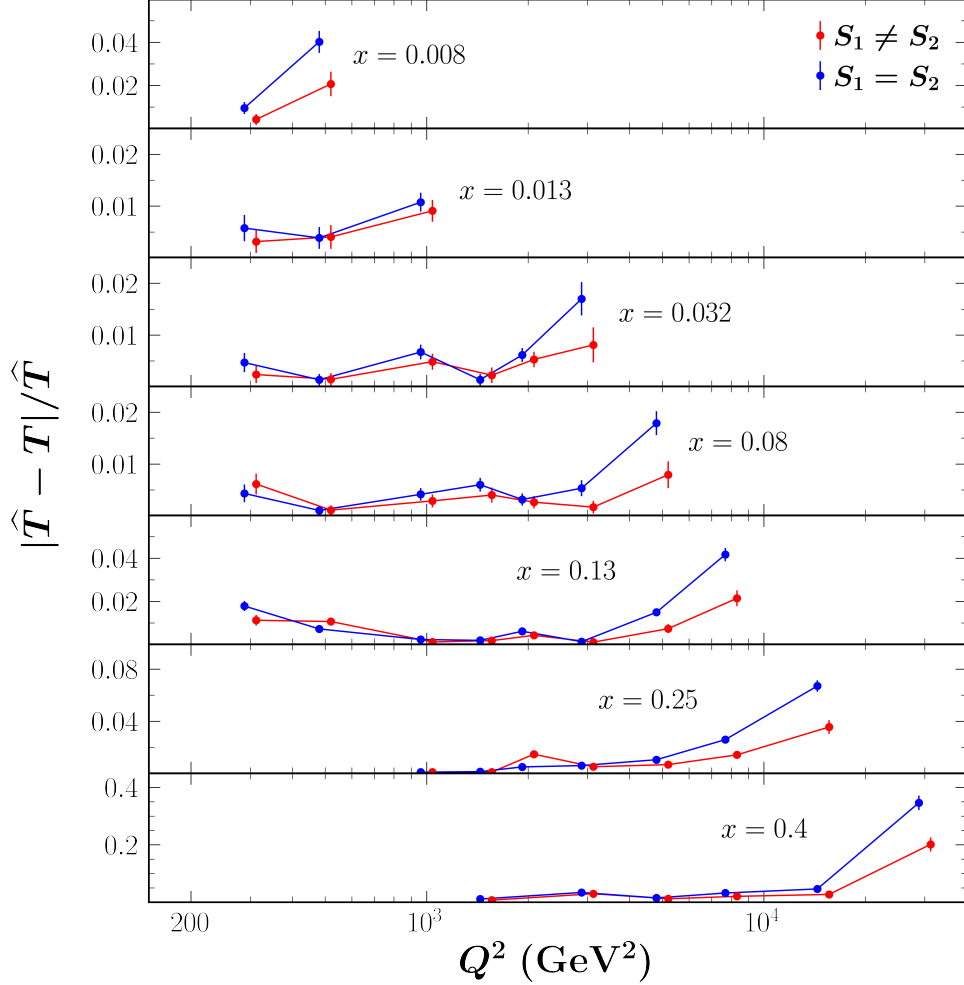


FIG. 9. Relative inferred systematic corrections  $|\hat{T} - T|/\hat{T}$ , as defined in Eq. (14), for the HERA charged current (CC)  $e^+p$  data as a function of  $Q^2$  for fixed  $x$  values using two model settings  $S_1 \neq S_2$  (red circles) and  $S_1 = S_2$  (blue circles).

insufficient parametrization flexibility in that analysis. In contrast, the SIDIS data primarily enhance  $s^+$  in the region  $x < 0.03$  relative to the baseline, while producing a monotonically decreasing behavior for  $R_s$  in the range  $0.01 < x < 0.3$ . Beyond this range, the uncertainties become too large to draw firm conclusions. The final results of the JAM24 scenario favor a strange quark suppression consistent with the +SIDIS scenario, likely due to the larger amount of SIDIS data (1228 points) compared to the  $W$ +charm data (37 points).

The incompatibility of  $s^+$  around  $x = 0.01$  between the baseline results and the alternative scenarios reflects a degree of bias and reduced variance in our underlying modeling. This



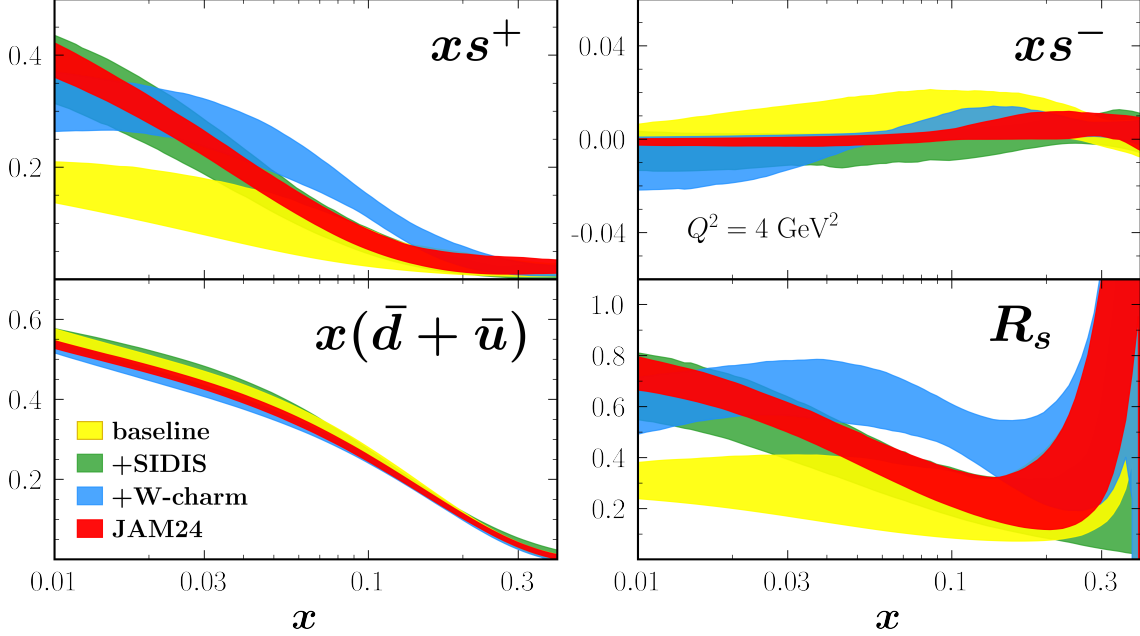


FIG. 10. Impact of the individual SIDIS (green bands) and  $W$ +charm (blue bands) data on the PDFs  $x s^+$ ,  $x s^-$ ,  $x(\bar{d} + \bar{u})$  and ratio  $R_s$  compared with the baseline fit (yellow bands) and the full JAM24 fit (red bands) that includes all of the data. Uncertainty bands represent a 95% credible interval at the scale  $Q^2 = 4 \text{ GeV}^2$ .

issue is particularly challenging in inverse problems, especially when the baseline datasets — aside from the HERA charged current data — do not provide direct constraints on the strange quark PDFs but offer only indirect constraints from sum rules and evolution effects.

However, once datasets such as the SIDIS kaon data and  $W$ +charm data are included, the bias is expected to be reduced. The fact that both datasets equally increase the strange quark PDF at  $x = 0.01$  suggests that the bias is indeed mitigated, at least in this region. At  $x = 0.1$ , however, the two datasets exhibit different pulls, highlighting the need for future data that are more sensitive to the strange quark PDF in this region. Such data could come from experiments at Jefferson Lab, including parity-violating DIS measurements and high-precision SIDIS multiplicity data from Halls B and C. Although QCD does not, in general, require the strange and anti-strange PDFs to be identical, the current datasets provide no clear indication of a nonzero  $s^- = s - \bar{s}$  asymmetry within the present uncertainties.

The results of our full global analysis for the PDFs are illustrated in Fig. 11, where we show each of the fitted PDFs at  $Q^2 = 4 \text{ GeV}^2$ . For comparison, we also show the results from

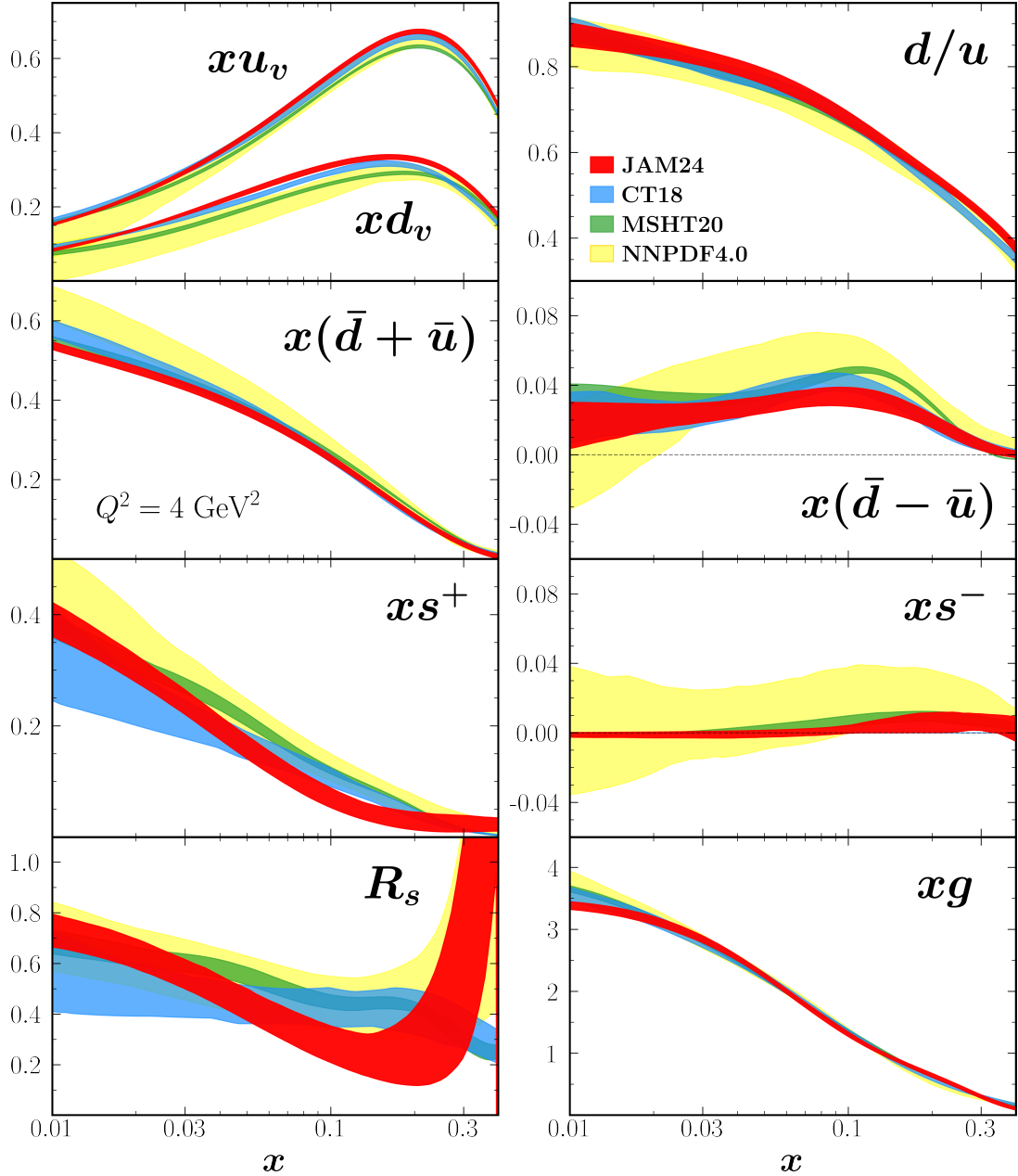


FIG. 11. Comparison of various PDFs from the present JAM24 global analysis (red bands) with results from the CT18 [74] (blue), MSHT20 [78] (green), and NNPDF4.0 [73] (yellow) NLO parametrizations at the scale  $Q^2 = 4 \text{ GeV}^2$ , with bands representing a 95% credible interval.

other NLO parametrizations, including the CT18 [74], MSHT20 [78] and NNPDF4.0 [73], with uncertainty bands representing the 95% credible interval. In these comparisons we focus on the kinematic region of parton momentum fractions  $0.01 \lesssim x \lesssim 0.4$  where the

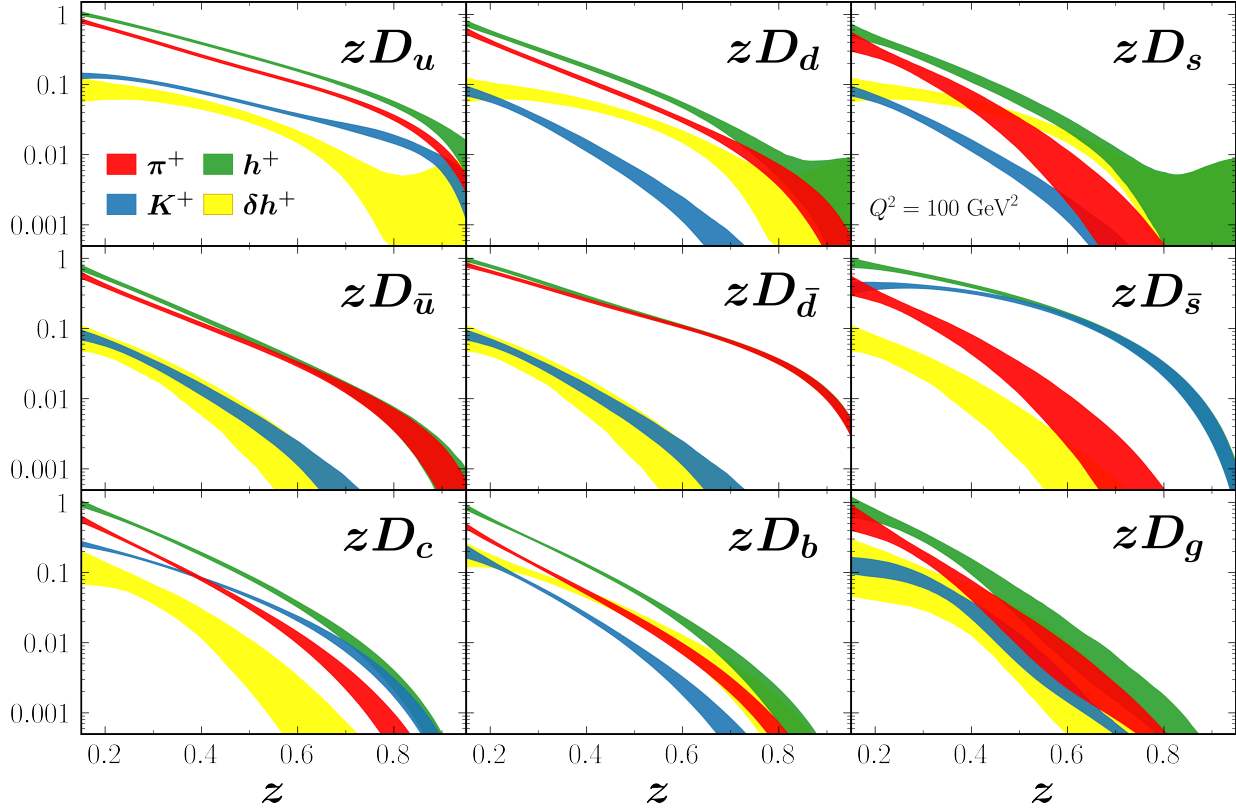


FIG. 12. Parton to hadron fragmentation functions  $zD_f$  versus  $z$  for the production of charged pions  $\pi^+$  (red bands), kaons  $K^+$  (blue), unidentified hadrons  $h^+$  (green), and residual hadrons  $\delta h^+$  (yellow) for 95% credible interval at  $Q^2 = 100 \text{ GeV}^2$ .

$W$ + charm and SIDIS datasets have the greatest impact on the strange quark PDF.

For the valence  $u$ - and  $d$ -quark distributions, as well as the  $d/u$  PDF ratio, our results are in overall agreement with those from other groups. Similarly, the light antiquark distributions  $\bar{d} + \bar{u}$  are generally consistent with other fit results, although our  $\bar{d} - \bar{u}$  distribution sits at the lower end of the other PDF sets in the intermediate- $x$  range. The total strange distribution,  $s^+$ , is in general agreement with other fits at low  $x$ , but has a smaller magnitude in the  $0.1 \lesssim x \lesssim 0.2$  range. This is also seen with the strange to nonstrange sea quark ratio,  $R_s$ , which is  $0.72^{+0.07}_{-0.06}$  at  $x = 0.01$ , but falls to  $0.20^{+0.21}_{-0.08}$  at  $x = 0.2$ .

For the FFs extracted in our analysis, in Fig. 12 we show the  $z$  dependence for positively charged  $\pi^+$ ,  $K^+$ , unidentified hadrons  $h^+$ , and residual hadrons  $\delta h^+$  defined in Eq. (12) at a scale  $Q^2 = 100 \text{ GeV}^2$ , for a 95% credible interval. Since the pion is the lightest hadron, as expected we find the magnitude of the  $\pi^+$  FFs is generally greater than those for kaons

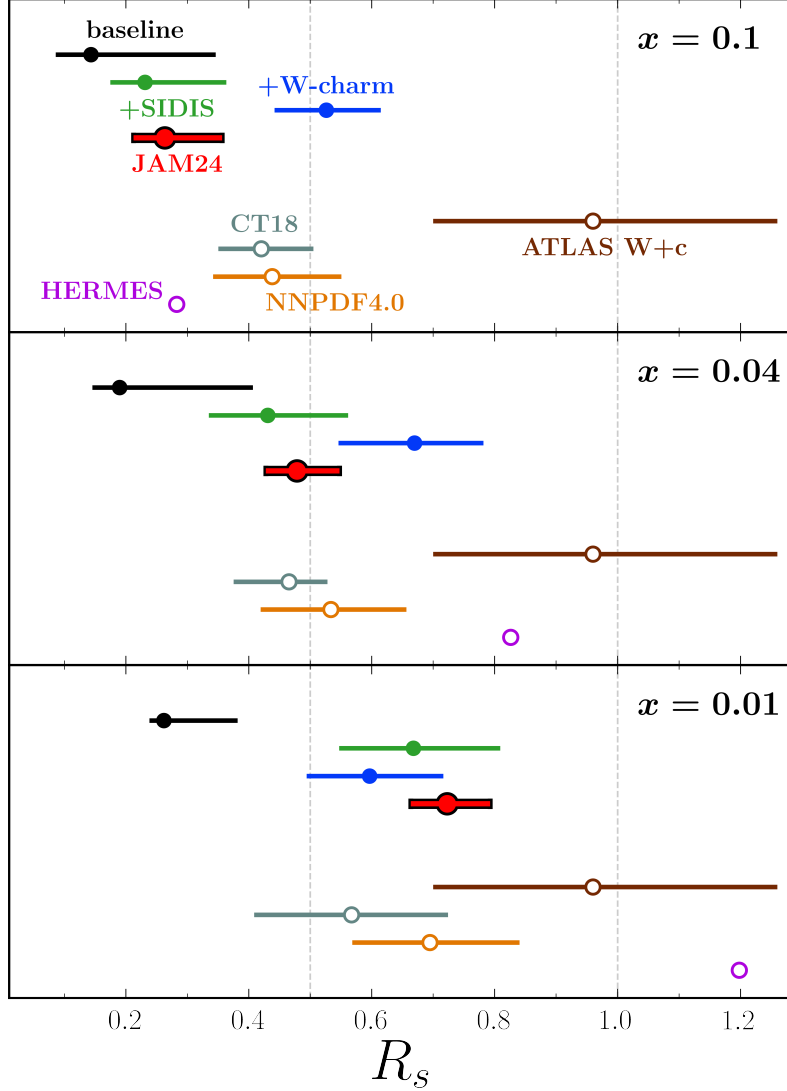


FIG. 13. Strange to nonstrange PDF ratio  $R_s$  at  $x = 0.1$  (top),  $x = 0.04$  (middle), and  $x = 0.01$  (bottom) at  $Q^2 = 1.9 \text{ GeV}^2$  for ATLAS  $W$ +charm [26] data (which show  $r_s = (s + \bar{s})/2\bar{d}$ ),  $Q^2 = 2.5 \text{ GeV}^2$  for HERMES data [14], and  $Q^2 = 4 \text{ GeV}^2$  for all other fits [73, 74]. The main JAM24 results (red circles) are compared with various other scenarios and analyses.

and other hadrons for most quark flavors. The exceptions to this are the FFs for  $\bar{s} \rightarrow K^+$ ,  $c \rightarrow K^+$  for intermediate  $z$ , and  $s \rightarrow \delta h^+$  also at intermediate  $z$ . Additionally, the  $b \rightarrow \delta h^+$  FF is comparable to that for  $b \rightarrow \pi^+$  in the intermediate- $z$  region. These findings are consistent with those found in previous JAM analyses [35, 69] and by other groups [79].

A summary of our findings for the strange to nonstrange ratio  $R_s$  is shown in Fig. 13,

where we compare the  $R_s$  values at  $x = 0.01$ ,  $x = 0.04$ , and  $x = 0.1$  for  $Q^2 = 4 \text{ GeV}^2$  with a 95% credible interval, from all the fits considered in this analysis, namely, the baseline, +SIDIS, + $W$ -charm, and the full JAM24 analysis. These are also compared with results from other PDF analyses, including the CT18 [74] and NNPDF4.0 [73], at the same  $x$  and  $Q^2$ . For the final JAM24 result, we find a strange to nonstrange sea quark ratio of  $R_s = 0.72_{-0.06}^{+0.07}$  at  $x = 0.01$  to be compatible with other fits in this analysis and results from other groups, with the exception of our baseline fit, which does not contain the SIDIS or  $W$ +charm datasets. In the intermediate- $x$  region, we find a more suppressed strange-quark PDF, with a ratio  $R_s = 0.48_{-0.05}^{+0.07}$  at  $x = 0.04$  and  $R_s = 0.26_{-0.05}^{+0.09}$  at a higher  $x = 0.1$ . This is again compatible with most other fits at these kinematics, with the exception of the + $W$ -charm fit which prefers an enhanced strange quark PDF at intermediate  $x$ .

## V. CONCLUSIONS

How “strange” is the proton has been a question that has perplexed nuclear and particle physicists for decades, attracting considerable experimental and theoretical attention in the quest to understand the detailed structure of the proton’s sea quarks, and in particular the size of the strange sea relative to the light antiquark sea. In this study we have for the first time performed a comprehensive global QCD analysis of the effect on the strange quark PDF in the proton from simultaneously including  $W$ +charm production data in  $pp$  collisions at the LHC and hadron production data in semi-inclusive muon-deuterium scattering from COMPASS, both of which are expected to have sensitivity to the  $s$  and  $\bar{s}$  distributions. The SIDIS data in particular require a simultaneous fit to both unpolarized PDFs and parton to hadron FFs.

An excellent overall reduced  $\chi^2$  value of  $\chi_{\text{red}}^2 = 1.07$  is obtained for the global fit, which includes datasets from DIS, Drell-Yan, weak boson and jet production, SIDIS, and SIA reactions, comprising over 5000 data points. It is the first time that such a large body of data, constraining both PDFs and FFs, has been successfully described within a collinear QCD factorization framework. We find  $\chi_{\text{red}}^2 \lesssim 1$  for both the LHC  $W$ +charm datasets, and the COMPASS SIDIS data on  $\pi^\pm$ ,  $K^\pm$ , and  $h^\pm$  lepton production.

In comparison to a baseline global fit that does not include these datasets, we find that the SIDIS and  $W$ +charm data combined favor a larger strange distribution, while SIDIS data

alone allow for a broader range of strange quark PDFs. Without SIDIS data the  $s^+$  PDF is larger at  $0.03 \lesssim x \lesssim 0.2$  than the combined fit, while at smaller  $x$  values the  $W$ +charm data have a stronger upward pull on  $s^+$  compared with the SIDIS data. Combined, the strange to nonstrange sea quark distribution ratio is  $R_s \approx \{0.72, 0.48, 0.26\}$  for  $x = \{0.01, 0.04, 0.1\}$ . We therefore conclude that the global dataset does not support an SU(3) flavor symmetric sea, but indicates strong SU(3) breaking at intermediate  $x$  values,  $x \gtrsim 0.01$ . We also do not find evidence from the current data for an  $s - \bar{s}$  asymmetry in the proton within the current uncertainties.

In the future our analysis can be extended in several ways. Firstly, we plan to include inclusive  $pp \rightarrow hX$  data to better constrain the FFs, supplementing the constraints from SIA and SIDIS. We will also explore the possibility of using new lattice QCD simulations of PDF moments and pseudo-Ioffe time distributions to provide complementary constraints on the  $s$  and  $\bar{s}$  distributions. Future data that will help with reconstructing the  $s$  and  $\bar{s}$  distributions will include parity-violating DIS, which gives access to a new combination of  $u^+$ ,  $d^+$  and  $s^+$  PDFs, as well as SIDIS for pion and kaon production at Jefferson Lab, with a 12 GeV and possibly a 22 GeV electron beam, as well as the Electron-Ion Collider. Finally, a definitive analysis will also include neutrino-nucleus DIS data, which historically been used to constrain the strange-quark PDF, with a systematic treatment of nuclear and hadronization uncertainties.

## ACKNOWLEDGMENTS

We thank Rabah Abdul Khalek, Patrick Barry, Chris Cocuzza, and Emanuele Nocera for helpful discussions and communications. This work was supported by the DOE contract No. DE-AC05-06OR23177, under which Jefferson Science Associates, LLC operates Jefferson Lab. T.A. acknowledges support from JSA/JLab Graduate Fellowship Program. The work of N.S. was supported by the DOE, Office of Science, Office of Nuclear Physics in the Early Career Program.

- 
- [1] A. W. Thomas, *Phys. Lett. B* **126**, 97 (1983).
- [2] R. S. Towell *et al.*, *Phys. Rev. D* **64**, 052002 (2001).
- [3] J. Dove *et al.*, *Nature* **590**, 561 (2021), [Erratum: *Nature* **604**, E26 (2022)].
- [4] C. Cocuzza, W. Melnitchouk, A. Metz, and N. Sato, *Phys. Rev. D* **104**, 074031 (2021).
- [5] A. I. Signal and A. W. Thomas, *Phys. Lett. B* **191**, 205 (1987).
- [6] X. Ji and J. Tang, *Phys. Lett. B* **362**, 182 (1995).
- [7] W. Melnitchouk and M. Malheiro, *Phys. Rev. C* **55**, 431 (1997).
- [8] A. O. Bazarko *et al.*, *Z. Phys. C* **65**, 189 (1995).
- [9] D. Mason *et al.*, *Phys. Rev. Lett.* **99**, 192001 (2007).
- [10] A. Kayis-Topaksu *et al.*, *New J. Phys.* **13**, 093002 (2011).
- [11] O. Samoylov *et al.*, *Nucl. Phys. B* **876**, 339 (2013).
- [12] N. Kalantarians, C. E. Keppel, and M. E. Christy, *Phys. Rev. C* **96**, 032201 (2017).
- [13] A. Accardi, F. Arleo, W. K. Brooks, D. D’Enterria, and V. Muccifora, *Riv. Nuovo Cim.* **32**, 439 (2009).
- [14] A. Airapetian *et al.*, *Phys. Lett. B* **666**, 446 (2008).
- [15] A. Airapetian *et al.*, *Phys. Rev. D* **89**, 097101 (2014).
- [16] M. Stolarski, *Phys. Rev. D* **92**, 098101 (2015).
- [17] E. Leader, A. V. Sidorov, and D. B. Stamenov, *Phys. Rev. D* **90**, 054026 (2014).
- [18] E. Leader, A. V. Sidorov, and D. B. Stamenov, *Phys. Rev. D* **93**, 074026 (2016).
- [19] S. Chatrchyan *et al.*, *JHEP* **04**, 050 (2011).
- [20] S. Chatrchyan *et al.*, *Phys. Rev. Lett.* **109**, 111806 (2012).
- [21] S. Chatrchyan *et al.*, *Phys. Rev. D* **90**, 032004 (2014).
- [22] M. Aaboud *et al.*, *Eur. Phys. J. C* **77**, 367 (2017).
- [23] V. Khachatryan *et al.*, *Eur. Phys. J. C* **76**, 469 (2016).
- [24] G. Aad *et al.*, *Phys. Rev. Lett.* **109**, 012001 (2012).
- [25] S. Chatrchyan *et al.*, *JHEP* **02**, 013 (2014).
- [26] G. Aad *et al.*, *JHEP* **05**, 068 (2014).
- [27] A. M. Sirunyan *et al.*, *Eur. Phys. J. C* **79**, 269 (2019).
- [28] M. Aaboud *et al.*, *Eur. Phys. J. C* **78**, 110 (2018), [Erratum: *Eur. Phys. J. C* **78**, 898 (2018)].

- [29] S. Alekhin, J. Blümlein, and S. Moch, *Phys. Lett. B* **777**, 134 (2018).
- [30] J. M. Campbell and R. K. Ellis, *Phys. Rev. D* **60**, 113006 (1999).
- [31] Y. L. Dokshitzer, *Sov. Phys. JETP* **46**, 641 (1977).
- [32] V. N. Gribov and L. N. Lipatov, *Sov. J. Nucl. Phys.* **15**, 438 (1972).
- [33] G. Altarelli and G. Parisi, *Nucl. Phys.* **B126**, 298 (1977).
- [34] S. Navas *et al.* (Particle Data Group), *Phys. Rev. D* **110**, 030001 (2024).
- [35] E. Moffat, W. Melnitchouk, T. C. Rogers, and N. Sato, *Phys. Rev. D* **104**, 016015 (2021).
- [36] L. W. Whitlow, E. M. Riordan, S. Dasu, S. Rock, and A. Bodek, *Phys. Lett. B* **282**, 475 (1992).
- [37] A. C. Benvenuti *et al.*, *Phys. Lett. B* **237**, 592 (1990).
- [38] M. Arneodo *et al.*, *Nucl. Phys.* **B483**, 3 (1997).
- [39] M. Arneodo *et al.*, *Nucl. Phys.* **B487**, 3 (1997).
- [40] H. Abramowicz *et al.*, *Eur. Phys. J. C* **75**, 580 (2015).
- [41] C. Adolph *et al.*, *Phys. Lett. B* **764**, 1 (2017).
- [42] C. Adolph *et al.*, *Phys. Lett. B* **767**, 133 (2017).
- [43] R. Aaij *et al.*, *JHEP* **12**, 079 (2014).
- [44] R. Aaij *et al.*, *JHEP* **01**, 155 (2016).
- [45] V. M. Abazov *et al.*, *Phys. Rev. Lett.* **112**, 151803 (2014), [Erratum: *Phys. Rev. Lett.* **114**, 049901 (2015)].
- [46] T. Aaltonen *et al.*, *Phys. Rev. Lett.* **102**, 181801 (2009).
- [47] J. Adam *et al.*, *Phys. Rev. D* **103**, 012001 (2021).
- [48] V. M. Abazov *et al.*, *Phys. Rev. D* **76**, 012003 (2007).
- [49] T. A. Aaltonen *et al.*, *Phys. Lett. B* **692**, 232 (2010).
- [50] V. M. Abazov *et al.*, *Phys. Rev. Lett.* **101**, 062001 (2008).
- [51] A. Abulencia *et al.*, *Phys. Rev. D* **75**, 092006 (2007).
- [52] B. I. Abelev *et al.*, *Phys. Rev. Lett.* **97**, 252001 (2006).
- [53] R. Brandelik *et al.*, *Phys. Lett. B* **100**, 357 (1981).
- [54] M. Althoff *et al.*, *Z. Phys. C* **22**, 307 (1984).
- [55] W. Braunschweig *et al.*, *Z. Phys. C* **42**, 189 (1989).
- [56] X.-Q. Lu, *Heavy quark jets from  $e^+e^-$  annihilation at 29 GeV*, thesis, Johns Hopkins University (1986).



- [57] H. Aihara *et al.*, [Phys. Rev. Lett. \*\*52\*\*, 577 \(1984\)](#).
- [58] H. Aihara *et al.*, [Phys. Rev. Lett. \*\*61\*\*, 1263 \(1988\)](#).
- [59] M. Derrick *et al.*, [Phys. Rev. D \*\*35\*\*, 2639 \(1987\)](#).
- [60] R. Itoh *et al.*, [Phys. Lett. B \*\*345\*\*, 335 \(1995\)](#).
- [61] K. Abe *et al.*, [Phys. Rev. D \*\*69\*\*, 072003 \(2004\)](#).
- [62] D. Buskulic *et al.*, [Z. Phys. C \*\*66\*\*, 355 \(1995\)](#).
- [63] R. Akers *et al.*, [Z. Phys. C \*\*63\*\*, 181 \(1994\)](#).
- [64] G. Abbiendi *et al.*, [Eur. Phys. J. C \*\*16\*\*, 407 \(2000\)](#).
- [65] P. Abreu *et al.*, [Eur. Phys. J. C \*\*5\*\*, 585 \(1998\)](#).
- [66] J. P. Lees *et al.*, [Phys. Rev. D \*\*88\*\*, 032011 \(2013\)](#).
- [67] M. Leitgab *et al.*, [Phys. Rev. Lett. \*\*111\*\*, 062002 \(2013\)](#).
- [68] H. Albrecht *et al.*, [Z. Phys. C \*\*44\*\*, 547 \(1989\)](#).
- [69] N. Sato, C. Andres, J. J. Ethier, and W. Melnitchouk, [Phys. Rev. D \*\*101\*\*, 074020 \(2020\)](#).
- [70] C. Cocuzza, C. E. Keppel, H. Liu, W. Melnitchouk, A. Metz, N. Sato, and A. W. Thomas, [Phys. Rev. Lett. \*\*127\*\*, 242001 \(2021\)](#).
- [71] R. Hyndman and Y. Fan, [The American Statistician \*\*50\*\*, 361 \(1996\)](#).
- [72] M. Boglione, A. Dotson, L. Gamberg, S. Gordon, J. O. Gonzalez-Hernandez, A. Prokudin, T. C. Rogers, and N. Sato, [JHEP \*\*10\*\*, 122 \(2019\)](#), [arXiv:1904.12882 \[hep-ph\]](#).
- [73] R. D. Ball *et al.*, [Eur. Phys. J. C \*\*82\*\*, 428 \(2022\)](#), [arXiv:2109.02653 \[hep-ph\]](#).
- [74] T.-J. Hou, J. Gao, T. J. Hobbs, K. Xie, S. Dulat, M. Guzzi, J. Huston, P. Nadolsky, J. Pumplin, C. Schmidt, I. Sitiwaldi, D. Stump, and C.-P. Yuan, [Phys. Rev. D \*\*103\*\*, 014013 \(2021\)](#).
- [75] A. Accardi, T. Hobbs, and W. Melnitchouk, [JHEP \*\*11\*\*, 084 \(2009\)](#).
- [76] J. V. Guerrero, J. J. Ethier, A. Accardi, S. W. Casper, and W. Melnitchouk, [JHEP \*\*09\*\*, 169 \(2015\)](#).
- [77] J. V. Guerrero and A. Accardi, [Phys. Rev. D \*\*97\*\*, 114012 \(2018\)](#).
- [78] S. Bailey, T. Cridge, L. A. Harland-Lang, A. D. Martin, and R. S. Thorne, [Eur. Phys. J. C \*\*81\*\*, 341 \(2021\)](#), [arXiv:2012.04684 \[hep-ph\]](#).
- [79] M. Hirai, S. Kumano, T.-H. Nagai, and K. Sudoh, [Phys. Rev. D \*\*75\*\*, 094009 \(2007\)](#).